Systems/Circuits

A Virtual In Vivo Dissection and Analysis of Socioaffective Symptoms Related to Cerebellum-Midbrain Reward Circuitry in Humans

Linda J. Hoffman,[1] Julia M. Foley,[1] Josiah K. Leong,[2] Holly Sullivan-Toole,[1] Blake L. Elliott,[1] and Ingrid R. Olson[1]
[1]Department of Psychology and Neuroscience, Temple University, Philadelphia, Pennsylvania 19122 and [2]Department of Psychological Science, University of Arkansas, Fayetteville, Arkansas 72701

Emerging research in nonhuman animals implicates cerebellar projections to the ventral tegmental area (VTA) in appetitive behaviors, but these circuits have not been characterized in humans. Here, we mapped cerebello-VTA white matter connectivity in a cohort of men and women using probabilistic tractography on diffusion imaging data from the Human Connectome Project. We uncovered the topographical organization of these connections by separately tracking from parcels of cerebellar lobule VI, crus I/II, vermis, paravermis, and cerebrocerebellum. Results revealed that connections between the cerebellum and VTA predominantly originate in the right cerebellar hemisphere, interposed nucleus, and paravermal cortex and terminate mostly ipsilaterally. Paravermal crus I sends the most connections to the VTA compared with other lobules. We discovered a mediolateral gradient of connectivity, such that the medial cerebellum has the highest connectivity with the VTA. Individual differences in microstructure were associated with measures of negative affect and social functioning. By splitting the tracts into quarters, we found that the socioaffective effects were driven by the third quarter of the tract, corresponding to the point at which the fibers leave the deep nuclei. Taken together, we produced detailed maps of cerebello-VTA structural connectivity for the first time in humans and established their relevance for trait differences in socioaffective regulation.

Key words: **cerebellum; depression; diffusion imaging; dopamine; reward; ventral tegmental area**

Significance Statement

This is the first study in humans to identify the white matter connections between each deep cerebellar nucleus and the VTA in an anatomically detailed manner. Our findings are highly consistent with the rodent literature, showing strong conservation across species. This provides a foundation for direct translational research using chemogenetic and optogenetic methods in rodents to study neuropsychiatric disorders associated with this pathway. We identify a double dissociation of socioaffective functioning and cerebellar deep nuclei and sagittal segments, hinting at a mediolateral hierarchy of cerebellar function based on cerebellar phylogeny.

Received June 3, 2024; revised Aug. 23, 2024; accepted Aug. 26, 2024.

Author contributions: L.J.H., J.K.L., H.S-T., B.L.E., and I.R.O. designed research; L.J.H. and J.M.F. performed research; L.J.H. analyzed data; L.J.H., J.M.F., J.K.L., H.S-T., B.L.E., and I.R.O. wrote the paper.

This research includes calculations carried out on HPC resources supported in part by the National Science Foundation through major research instrumentation grant number 1625061 and by the US Army Research Laboratory under contract number W911NF-16-2-0189. This work was supported by a National Institute of Health Grant to I.R.O. (R01 NICHD R01HD099165; R01 MH118545-01A1) and to H.S-T. (F32 MH127948-01A1). The content is solely the responsibility of the authors and does not represent the official views of the National Institute of Mental Health or the National Institutes of Health. Data were provided by the Human Connectome Project, WU-Minn Consortium (Principal Investigators: David Van Essen and Kamil Ugurbil; 1U54MH091657) funded by the 16 NIH Institutes and Centers that support the NIH Blueprint for Neuroscience Research and by the McDonnell Center for Systems Neuroscience at Washington University. We thank Drs. Volker Coenen, Marco Reisert, and Sascha du Lac for their insights into cerebello-midbrain connectivity and comments on the cerebellar connections to each DCN, respectively. We also thank Katie Jobson, Haroon Popal, and Vishnu Murty for contributing their knowledge of cerebellar and reward circuitry.

The authors declare no competing financial interests.

Correspondence should be addressed to Linda J. Hoffman at linda.jasmine.hoffman@temple.edu.

https://doi.org/10.1523/JNEUROSCI.1031-24.2024

Introduction

The cerebellum is often overlooked by research on affective and motivated behaviors. However, over the last 20 years, neuroimaging studies have found cerebellar alterations in a range of neuropsychiatric disorders such as depression (Phillips et al., 2015), schizophrenia (Andreasen and Pierson, 2008; Moberget et al., 2018), autism spectrum disorder (ASD; Courchesne et al., 1988; Wang et al., 2014), and substance abuse (Moulton et al., 2014; Miquel et al., 2020). For instance, a recent study examined the new incidence of psychiatric disorders following the onset of cerebellar disease in older adults (Delle Chiaie et al., 2015). Results show that bipolar disorder was diagnosed in 31% of patients with cerebellar disease, highlighting the importance of the cerebellum in emotion regulation. Converging evidence from volumetric studies has found changes in cerebellar volume

in individuals with bipolar disorder relative to healthy controls (Lippmann et al., 1982; Nasrallah et al., 1982; DelBello et al., 1999; Mills et al., 2005; Baldacara et al., 2011; Kim et al., 2013; Eker et al., 2014; Lupo et al., 2021; see also Brambilla et al., 2002; Monkul et al., 2008; Laidi et al., 2015).

Mood disorders can be conceptualized as problems in reward-seeking or motivated behavior (Russo and Nestler, 2013; Gonen et al., 2014). New research has shown that the cerebellum may play an essential role in motivated behavior through its influence on the ventral tegmental area (VTA), a midbrain nucleus that plays a key role in motivated behavior as the origin of many dopaminergic cell bodies (Novello et al., 2022). Monosynaptic connectivity between the cerebellum and VTA has been established from axon tracer studies (Snider et al., 1976; Phillipson, 1979; Perciavalle et al., 1989; Watabe-Uchida et al., 2012; Judd et al., 2021) in cats and rodents as well as optogenetic investigations in mice (Carta et al., 2019; Baek et al., 2022). In a seminal study, Carta et al. (2019) transiently silenced the cerebello-VTA pathway in mice and found that stimuli that were usually rewarding—other mice—became uninteresting after optogenetically inactivating the pathway. Another study by Low et al. (2021) found that upregulating the pathway in mice could increase feeding behavior, while downregulating the pathway decreased feeding, regardless of baseline satiety. Moreover, selectively activating or silencing neurons projecting from the cerebellum could alter VTA activity such that more or less dopamine is released (Low et al., 2021). This suggests that portions of the cerebellum regulate reward signals that catalyze or inhibit reward-driven behavior, even without direct manipulation of central reward regions.

These findings suggest that the cerebello-VTA pathway may play an essential, yet overlooked, role in motivated behavior. Moreover, this circuit may be relevant to the pathophysiology of diverse socioaffective disorders with disrupted reward-seeking behavior including disorders with prominent reductions in social motivation, like social anxiety, schizophrenia, autism spectrum (ASD; Berridge and Robinson, 2016), eating, substance use (Berridge and Robinson, 2016; Morales and Berridge, 2020), and mood disorders (Watson and Naragon-Gainey, 2010; Pizzagalli, 2014). To date, no research has characterized the cerebello-VTA structural connectivity in a detailed fashion in humans.

In this study, we provide a detailed characterization of the cerebello-VTA pathway in humans. We performed tractography from each deep cerebellar nucleus, as well as the cerebellar cortex, to visualize and quantify this pathway in a granular manner. We also seeded within sagittal cerebellar cortical segments for the first time. We mapped the laterality and topographical organization of the projections cerebellar projections, restricting our analysis to cerebellar lobules VI, crus I and II, which are the only regions in the posterior lobe that have vermal regions corresponding to the neocerebellum (Amore et al., 2021) and which converge with the cerebellar regions linked functionally to reward processing (Popal, 2023). Finally, we tested the prediction that individual differences in cerebello-VTA tract microstructure would be associated with variability in social and affective function.

Materials and Methods

Data availability

White matter fiber orientation distributions, MNI and subject-level region of interest/exclusion masks, and tractography files may be furnished upon request. Raw MRI, demographic, and certain behavioral/self-report data are restricted by the National Institute of Health and the HCP. Because of this, access to restricted data must be requested by fulfilling out the HCP's Electronic Restricted Access Application. Finally, since much of the data in the current study is accessible to the larger research community, subject IDs will be available upon request. This also applies to data files containing macro- and microstructural indices for the tracts under study. Further, exemplar tractography scripts and statistical code, as well as any other information required to reanalyze the data reported in this paper, are available from the lead contact upon request. These materials will be furnished provided they will be used for an explicit research purpose, and the requester has access to the HCP dataset.

Participants

All imaging data were acquired from the minimally preprocessed S900 release of the Human Connectome Project (HCP) dataset. For in-depth details concerning data acquisition parameters, preprocessing, and quality control for this dataset, see Van Essen and colleagues (Marcus et al., 2011, 2013; Van Essen et al., 2012, 2013; Glasser et al., 2013; Sotiropoulos et al., 2013; Ugurbil et al., 2013). Our final cohort consisted of 101 individuals and is described in greater detail below.

Our goal was to have a sample size of ~100, evenly split between biological male and female participants, who varied in their raw Achenbach Adult Self-Report (ASR) depression and anxiety subscale scores. We did this to have sufficient variability on affectively relevant behavioral measures for planned follow-up investigations on individual differences in tract microstructure as it relates to emotion dysregulation. Further, we decided to use 101 subjects since our previous work performing cerebellar tractography on HCP data revealed that sampling ~100 individuals down from the whole sample of >600 subjects revealed a similar pattern of results (Metoki et al., 2022). This suggests that probabilistic tractography results in this dataset are reliable and robust when sampling a subset of the larger cohort. We also chose a sample of 101 individuals since we used a stratified random sampling approach based on anxiety and depression subscale scores for which there were no large amounts of men and women on the higher ends of the scale. While also matching subjects based on sex, this limited the available subjects for the cohort, as efforts were made to promote a balance of scores.

Candidate participants were eliminated from the dataset if they did not have diffusion-weighted scans or T1-weighted scans, were left-handed, or did not have complete ASR data. Once these factors were considered, even numbers of males and females were chosen. The remaining participants were ranked according to their raw ASR depression and anxiety subscale scores. Men and women at the low, middle, and high end of the ASR subscale were randomly selected in a balanced manner until an equal number of men and women were acquired. This was done by selecting those who had high raw scores on this ASR subscale, for whom the subject's scores were uniquely high (i.e., those for whom no ties were present on the ASR depression and anxiety subscale). From there, equal numbers of those for whom ties were present were randomly selected to ensure an egalitarian distribution of depression and anxiety scores. For example, if a woman with a raw ASR depression and anxiety subscale score of 12 was added, a male with a score of 12 was added, and so forth, until the complete sample was achieved. To clarify, those with low- and mid-level anxiety and depression scores were more abundant, and after those from the more uniquely "high" end of the ASR anxiety and depression subscale were selected, equal numbers of men and women for every other value were incorporated into the final cohort. In the end, the demographic makeup of our sample was 72% white, 14% black or African American, 9% Asian/Native American/Pacific Islander, 2% unknown or not reported, and 3% mixed race. The average age of our subjects was 28.56 with a standard deviation of 3.69. Finally, the median income for the sample was within the bracket of $40K–$49,999, a figure that was based on reporting from 99 of the 101 participants under study, as two subjects did not answer this question. After completing our final analysis, we noticed that nine pairs of siblings had been included. In later sections, we describe how we account for shared variance due to genetic relatedness.

To combat potential sex differences based on affective self-report, males and females were matched on the ASR anxiety and depression

subscale. However, in the case of our secondary self-report measure, the NEO Five-Factor Inventory (NEO-FFI), males and females could not be matched, and so follow-up analyses were performed controlling for sex in cases where a significant brain–behavior relation was identified. It is important to note that the current study did not make hypotheses regarding how race, ethnicity, or socioeconomic status may impact tract macro- or microstructure or how these factors may contribute to underlying anatomy or brain–behavior effects. As such, the current analyses should be replicated in the future with a more diverse cohort and a demographic-driven research question to ascertain whether these factors have an impact on anatomy and function.

Experimental design

Diffusion-weighted imaging methods. The cerebellar ROIs included the deep cerebellar nuclei (DCN)—the fastigial, interposed, and dentate nuclei (Purves et al., 2001; Rajasekhar, 2022)—and the cerebellar lobules VI, crus I and II. The ROIs were extracted from the Montreal Neurological Institute (MNI) probabilistic atlas for cerebellar lobules and deep nuclei (Diedrichsen et al., 2009, 2011; see also https://www.diedrichsenlab.org/imaging/propatlas.htm). To prevent overlapping voxel coverage between the ROIs, we thresholded at varying levels for neighboring ROIs (Table 1). Note that the cerebellar ROIs were registered to MNI space using *fnirt*, the resolution for the atlas was 2 mm, and the atlas selected was not prethresholded.

The cerebellar cortex has many distinct functional regions within each lobule, so we increased the granularity of our analysis by creating zebrin-informed sagittal segments of lobules VI, crus I and crus II. This was performed after setting the minimum threshold for each at 25 using the *fslmaths* command in FSL. This resulted in the left and right regions for each lobule that were 20 voxels and 25 voxels wide, respectively. Each left and right lobule was then partitioned into five-voxel segments along the *x*-axis, resulting in four segments per hemisphere for lobule VI, and five segments per hemisphere for crus I and II. This was done by determining the *x*-axis boundaries of each segment in MNI space and using the *fslroi* command to "zero-out" all cerebellar lobule voxels to the left and right of those boundaries. Sagittal divisions are labeled by number, with higher numbers indicating more lateral portions of each lobule. For the purposes of the current analysis, Segment 1 of the cerebellar lobules has been assigned the title of paravermis, or "spinocerebellum," due to its medial positioning immediately adjacent to the vermis. Thus, Segment b sends projections to the interposed nucleus (IN) in subsequent analyses. All other segments (i.e., c_1–c_3 for lobule VI and c_1–c_4 for crus I and II) are considered part of the cerebrocerebellum and therefore project to the dentate nucleus (DN).

Since the vermis contains subdivisions corresponding to each cerebellar lobule, and the particular portions of this structure that may be most important for social and affective functioning are still uncharted, for the sake of the current analysis, we only investigate portions of the vermis that correspond to the cerebellar lobules of interest. Note that all vermal projections synapse onto the fastigial nucleus (FN) before leaving the cerebellum.

Table 1. Thresholds for ROIs

Cerebellar cortex						
	Crus I		Crus II		Lobule VI	
	Hemisphere	Vermis	Hemisphere	Vermis	Hemisphere	Vermis
Left Right	25	1	25	20	25	20
Deep cerebellar nuclei						
	Fastigial nucleus		Interposed nucleus		Dentate nucleus	
Left Right	5		25		45	

These threshold values were fed into *fslmaths* using the *-thr* argument in order to yield the final ROI masks. Note that "left" and "right" indicate how the thresholds were applied across each cerebellar hemisphere. In every case, the thresholding was performed symmetrically.

Brainstem ROIs were extracted from the Brainstem Navigator Atlas, derived from 7 Tesla (T) in vivo magnetic resonance imaging (MRI) using multiple contrasts and segmentation methods (https://www.nitrc.org/projects/brainstemnavig/; Bianciardi et al., 2016). We used the bilateral VTA from this atlas as our target ROI and further used the red nucleus and inferior colliculus (IC) as exclusion masks in the tractography analyses described below.

To delineate these transformation parameters, a series of linear registrations were performed. First, subjects' T1-weighted images were skull-stripped using FSL's brain extraction tool, which executed a bias field and neck cleanup. Next, subjects' top up–corrected, time-collapsed b0 images were registered to their respective T1-weighted anatomical images with six degrees of freedom and a correlation ratio cost function, yielding a diffusion to structural space conversion matrix. The same registration parameters were used to warp subjects' T1-weighted images to the $2\times2\times2$ mm^3 MNI space brain template, creating a structural to standard space conversion file. Next, the inverse of the two aforementioned matrices was taken to produce a structural to diffusion space and a standard to structural space conversion matrix, respectively. Last, to acquire the diffusion to standard space transformation parameters, the structural to standard space and diffusion to structural space matrices were concatenated. Finally, the inverse of this file was taken to create the standard to diffusion space conversion matrix that was used to convert the spheres to subject space. This procedure was enacted to avoid performing transformations directly on images that transcend two different imaging modalities (i.e., T1-weighted and diffusion MRI). Finally, the MNI to diffusion space transformation matrix was used in conjunction with FSL's nonlinear registration tool, *fnirt*, to warp ROIs to diffusion space (Andersson et al., 2010).

Further, it is critical to note that one key aim of the current investigation was to reveal monosynaptic, direct connections between the cerebellum and VTA. This is challenging due to the proximity of the VTA to the red nucleus and thalamus, which are waypoints in the cerebello-thalamo-cortical tract (CTC)—the largest cerebellar output tract (Palesi et al., 2015). Therefore, to dissociate the cerebello-VTA pathway from the CTC, we excluded the thalamus and red nucleus bilaterally. To prevent overlap with the VTA, the VTA was subtracted from the red nucleus once in the subject space, and the difference was used in the exclusion mask.

To ensure extraneous fibers were not reconstructed as part of this investigation, we also excluded the brainstem inferior to, and including the pons, the cerebellum contralateral to where each tractography was seeded, the VTA contralateral to that being targeted, and all lobes of the cerebral cortex. In the case of the decussating tract, we forced decussation at the level of the IC via the Wernekink commissure. To do this, we identified the last slice of the IC ROIs from the Brainstem Navigator Atlas in the MNI space and excluded all voxels superior to that slice in the hemisphere ipsilateral to the cerebellar seed region.

MRTrix3 (https://www.mrtrix.org/) was used to estimate voxel-wise response functions for each principal neural tissue compartment, including gray matter, white matter, and cerebral spinal fluid, using the *dhollander* algorithm (Dhollander et al., 2016, 2018, 2019). We fit multitissue orientation distribution functions for each macroscopic tissue type using the *msmt_csd* argument in the *dwi2fod* command. This approach capitalized on the distinct diffusion properties of different tissue types measured by the multi-b-value, high angular resolution diffusion imaging (HARDI) sequence in the HCP (Jeurissen et al., 2014).

Probabilistic tractography was performed using the iFOD2 algorithm in MRTrix3 using the *tckgen* command in subjects' native space. Note that for all tractographies, streamline selection criteria were disabled. Further, all tractographies seeded in the cerebellar cortex were performed unidirectionally, with the VTA designated as both an inclusion and stopping criteria. To make conjectures about tract density, we seeded a fixed number of streamlines per voxel in the seed mask, with random placement of the seeds throughout. To control for differing seed size of distinct cerebellar cortical areas, we determined the lowest volumetric occurrence of any of the cortical seed regions within the cohort. We found the smallest size in any subject to be that of the vermis corresponding to right crus II, with a volume of 329 voxels. Using 5,000 seeding attempts per voxel as

our default selection criteria, we calculated the total number of viable seeds for all lobule-based tractographies by multiplying 329 voxels by 5,000 seed attempts per voxels, resulting in 1,645,000 total seeds for each tractography. The seeding attempts per voxel for all other lobule-based tractographies were anchored by the smallest volumetric occurrence for each seed in the cohort and were calculated by dividing the smallest seed volume for each tractography in our sample by 1,645,000 total seeds. This information is summarized in Table 2.

For tractographies seeded in the DCN, tracking was performed unidirectionally. Due to the small size of the DCN relative to the portions of the cerebellar cortex under study, the total number of seeds was anchored at the smallest occurrence of any of the DCN. In this case, the smallest nucleus was found in a subject whose right fastigial nucleus was 91 voxels. Therefore, for all DCN tractographies, the total number of seeds was set at 91 voxels × 5,000 seeding attempts per voxel, yielding a total seed count of 455,000 for each tractography. The value of seeds per voxel for all other DCN-seeded tractographies was determined by dividing the smallest occurrence of each DCN in the cohort, divided by the total number of seeds (455,000). This information is summarized in Table 2. Subject-wise streamlines and tract length were extracted using the mrVista package (https://github.com/vistalab/vistasoft) in MATLAB version 2017b (9.3).

Note that we are able to make claims regarding the directionality of the tract based on ground truth neuroanatomical tracer studies that have identified the DCN as the primary outputs of the cerebellar cortex, which in turn, receive modulatory signals from Purkinje cells in the cerebellar cortex (Purves et al., 2001; Cohen, 2013; Novello et al., 2022). This informed our decision to use the cerebellar cortex and DCN as starting points for our tractographies, although we stress that diffusion imaging techniques do not allow us to infer the true directionality of reconstructed fibers. While it is reasonable to surmise that the majority of the fibers under study represent cerebellar efferents, some proportions of this tract may also consist of afferents from the midbrain.

Further, polysynaptic tracts (i.e., those originating in the cerebellar cortex, synapsing onto the DCN, and terminating in the VTA) from regions found to have the highest density of streamlines, as well as each monosynaptic tract seeded in each DCN, were split into 100 nodes using Automated Fiber Quantification through Python (PyAFQ; Kruper et al., 2021). That is, tractography between the cerebellum and VTA was funneled into PyAFQ, which split the tracts into 100 equidistant nodes. We then extracted the diffusion metric, fractional anisotropy (FA), at each node, for each tract, for every subject. Therefore, different "FA tract profiles" were output for each subject (Yeatman et al., 2012). This is important as FA values are not the same along the whole tract, so in averaging across the entirety of the tract, systematic variability across each bundle is diminished. Further, to get a total FA profile for each tract, FA was averaged across each of the 100 nodes. Then, to delve deeper into the portions of each tract that were found to correlate with self-report indices, we split the 100 nodes into four quarters by averaging FA every 25 nodes. In keeping with the data-driven approach and to reduce the number of multiple comparisons in the current analysis, FA in the right-seeded ipsilaterally traveling tracts was quantified, as these tracts were found to have the highest density of streamlines traveling to the VTA.

Table 2. ROI and tractography parameters

Polysynaptic anchor and tractography parameters												
Crus I												
	Segment											
	a		b		c_1		c_2		c_3		c_4	
Hemisphere	Anc. Vol	Seeds/vox	Anc. Vol	Seeds/vox	Anc. Vol	Seeds/vox	Anc. Vol	Seeds/vox	Anc. Vol	Seeds/vox	Anc. Vol	Seeds/vox
Left	795	2,069	870	1,891	1,437	1,145	2,337	704	3,397	484	2,346	701
Right	502	3,277	898	1,832	1,522	1,081	2,449	672	3,510	469	2,349	700
Crus II												
	Segment											
	a		b		c_1		c_2		c_3		c_4	
Hemisphere	Anc. Vol	Seeds/vox	Anc. Vol	Seeds/vox	Anc. Vol	Seeds/vox	Anc. Vol	Seeds/vox	Anc. Vol	Seeds/vox	Anc. Vol	Seeds/vox
Left	407	4,042	1,531	1,074	1,757	936	1,689	974	2,218	742	1,725	954
Right	329	5,000	1,287	1,278	1,820	904	1,692	972	1,907	863	1,686	976
Lobule VI												
	Segment											
	a		b		c_1		c_2		c_3			
Hemisphere	Anc. Vol	Seeds/vox	Anc. Vol	Seeds/vox	Anc. Vol	Seeds/vox	Anc. Vol	Seeds/vox	Anc. Vol		Seeds/vox	
Left	1,262	1,303	1,445	1,138	2,180	755	2,589	635	1,221		1,347	
Right	964	1,706	1,433	1,148	2,072	794	2,451	671	1,093		1,505	
Monosynaptic anchor and tractography parameters												
	Deep cerebellar nuclei											
	Fastigial nucleus				Interposed nucleus				Dentate nucleus			
Hemisphere	Anc. Vol		Seeds/vox		Anc. Vol		Seeds/vox		Anc. Vol		Seeds/vox	
Left	94		4,840		203		2,241		322		1,413	
Right	91		5,000		199		2,286		318		1,431	

The anchor volume for each seed region is reported in voxels. Seeds per voxel were calculated by dividing the anchor volume in voxels by 1,645,000 in the case of the polysynaptic tractography and by 455,000 in the case of the monosynaptic tractography. Anc, anchor; Vol, volume; vox, voxel.

Based on known neuroanatomy, we can make some assumptions about each quarter. For the polysynaptic tracts, quarter one (Q1) likely corresponds to the granule cells, parallel fibers, and Purkinje cell fibers in the molecular and Purkinje cell layers. Quarter two (Q2) corresponds to the granular layer containing Purkinje cell axons and climbing fibers at the juncture where these projections hit the DCN. Quarter three (Q3) corresponds to the mossy fibers and DCN outputs converging on the superior cerebellar peduncles. Finally, quarter four (Q4) corresponds to the point of VTA innervation in the midbrain. The anatomical breakdown of the quarters for the polysynaptic tracts is exemplified in a representative tract in Figure 1.

For the monosynaptic tracts, Q1 is the point of departure from the DCN within the cerebellum. Q2 and Q3 reflect the inferior and superior portions of the superior cerebellar peduncles, respectively. Finally, Q4 is the point of VTA innervation in the midbrain.

Self-report measures. To assess associations between tract microstructure and psychiatric and life function in the domains of negative affect, anxiety, depression, and social support, we examined measures form the ASR for ages 18–59. To explore specific domains of functioning, we examined ASR syndrome scales as quantified by the 123 items from Section VIII of the assessment. We predicted we would see correlations between anxiety and depression, social withdrawal, and internalizing symptom subscales. In a set of exploratory investigations, we also assessed associations with somatic complaints and attention problems. Finally, we evaluated correlations between externalizing symptoms and aggressive behavior as control analyses. Since this is a normative sample, we probed for associations using raw scores instead of age- and/or gender-adjusted percentile scores to retain sufficient variability to detect effects.

Next, to examine relations between tract microstructure and socially and affectively relevant personality traits, we looked at correlations with the NEO-FFI, a shortened, 60-item version of the original five-factor assessment (Costa and McRae). The FFI has exhibited strong reliability and validity cross-culturally and is thought to reflect key components of human personality (McCrae and Costa, 2004; Heine and Buchtel, 2009). In the current analysis, we looked at scores on neuroticism (N), extroversion/introversion (E), and agreeableness (A) subscales as outcomes of interest, as these measures provide insights into stable measures of emotional (N) and social (E and A) functioning. As a control outcome, we examine correlations with trait conscientiousness (C), as it is orthogonal to socioaffective disposition.

Statistical analyses

All statistical analyses for the anatomical aims were performed in RStudio version 1.4.1717 (https://www.r-project.org/). For the brain self-report analyses, statistics were performed in JASP version 0.18, a graphical user interface–based software whose engine runs in R. Finally, checks for robustness controlling for genetic relatedness in the individual difference analyses were followed up in R.

Anatomical analyses. Focused, pairwise contrasts were performed to ascertain the following comparisons pertaining to tract density: (1) contralaterally versus ipsilaterally synapsing tracts, performed for each cerebellar segment; (2) right- versus left-traveling tracts; (3) vermal versus paravermal, vermal versus cerebrocerebellar, and paravermal versus cerebrocerebellar tracts; (4) tracts originating in crus I versus crus II, crus I versus lobule VI, and crus II versus lobule VI; (5) projections to the VTA from the dentate nucleus versus interposed nucleus, dentate nucleus versus fastigial nucleus, and interposed nucleus versus fastigial nucleus. All contrasts were performed using paired Wilcoxon signed-rank tests in the *rstatix* package. To get effect sizes, we used the *wilcox_effsize()* command. Moreover, we computed 95% percentile confidence intervals bootstrapped around the effect size using 10,000 iterations using the "perc" argument. In all cases, the effect size "*r*" was calculated for all analyses (for documentation on the wilcox_effsize() command, see https://cran.r-project.org/web/packages/rstatix/rstatix.pdf).

Note that the results for the polysynaptic circuitry are presented in three different ways: (1) without any controls; (2) after controlling for the size of the DCN ROI in each projection route (dividing the

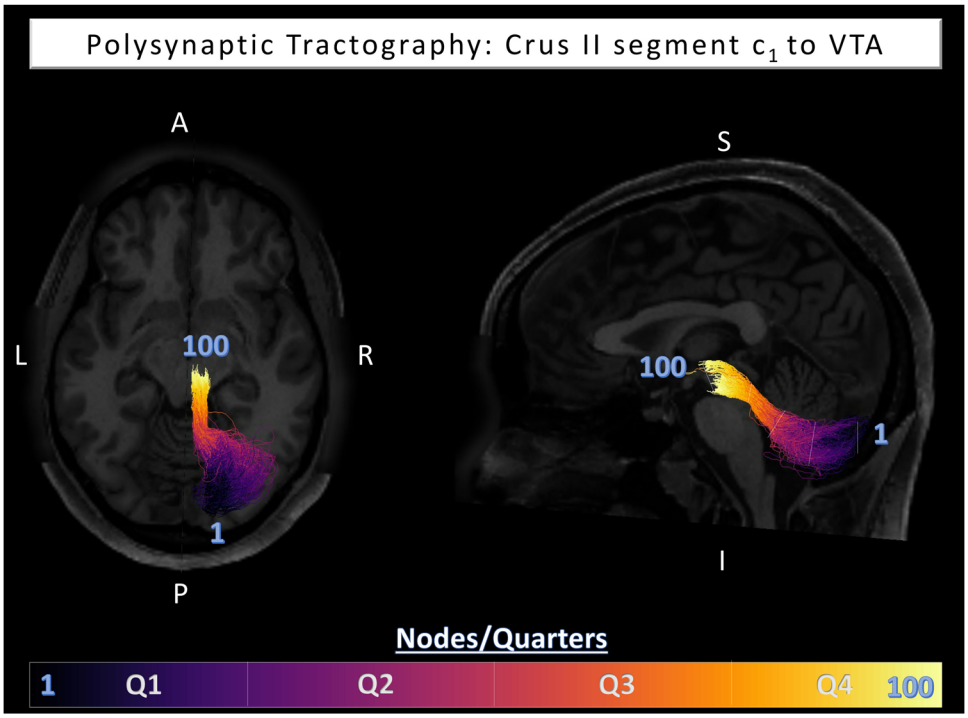

Figure 1. Visualization for a representative polysynaptic tractography originated in crus II of segment c_1 of the cerebrocerebellum, overlaid on a T1-weighted image. The number 1 indicates where the node-wise segmentation originated, while 100 represents where the segmentation ended. The boundaries of each quarter are indicated by white lines on the sagittal view of the tract, and the color coding corresponding to each quarter is summarized in the color bar at the bottom of the figure. In cases of monosynaptic tractographies that were also split into quarters, this segmentation involves the equal quarterization of Q3 and Q4 visualized above, although they are not visualized in the current figure. That is, the monosynaptic quarters correspond to Q3–4 in the current illustration.

number of streamlines for each tract by the volume of the relevant DCN ROI on a subject-wise basis); and (3) after controlling for tract length (dividing the number of streamlines by tract length). In this way, DCN ROI volume and tract length are treated as potential confounds, and the extent to which the three results converge is assessed to ascertain the relative importance of each in relation to our findings. For a visualization of the tractographies performed in the current analysis, see Figure 2.

Brain self-report analyses. Bivariate nonparametric Spearman correlations are reported for all analyses between tract segment FA and ASR and NEO-FFI personality traits. Follow-up exploratory quarter-wise tract correlations with behavior were also performed in a bivariate fashion. Moreover, the frequency of each quarter's emergence as the driver of the overall brain–behavior effect in question was investigated. For correlations between tract microstructure and NEO-FFI measures on which subjects were not able to be matched by sex, partial correlations controlling for sex were performed. Since the groups were matched for sex on the ASR, and since age was not a confound in the case of the ASR or NEO-FFI, neither multivariate regressions nor partial correlations were performed.

We took a data-driven approach to select tracts for analysis. In short, we performed follow-up brain self-report analyses only on tract segments for which there was the highest likelihood of structural connections existing and for which the connections were the most robust. We based these decisions on the anatomical analyses described in previous sections, making these determinations based on (1) the originating cerebellar hemisphere; (2) the direction of the traveling fibers (i.e., whether they

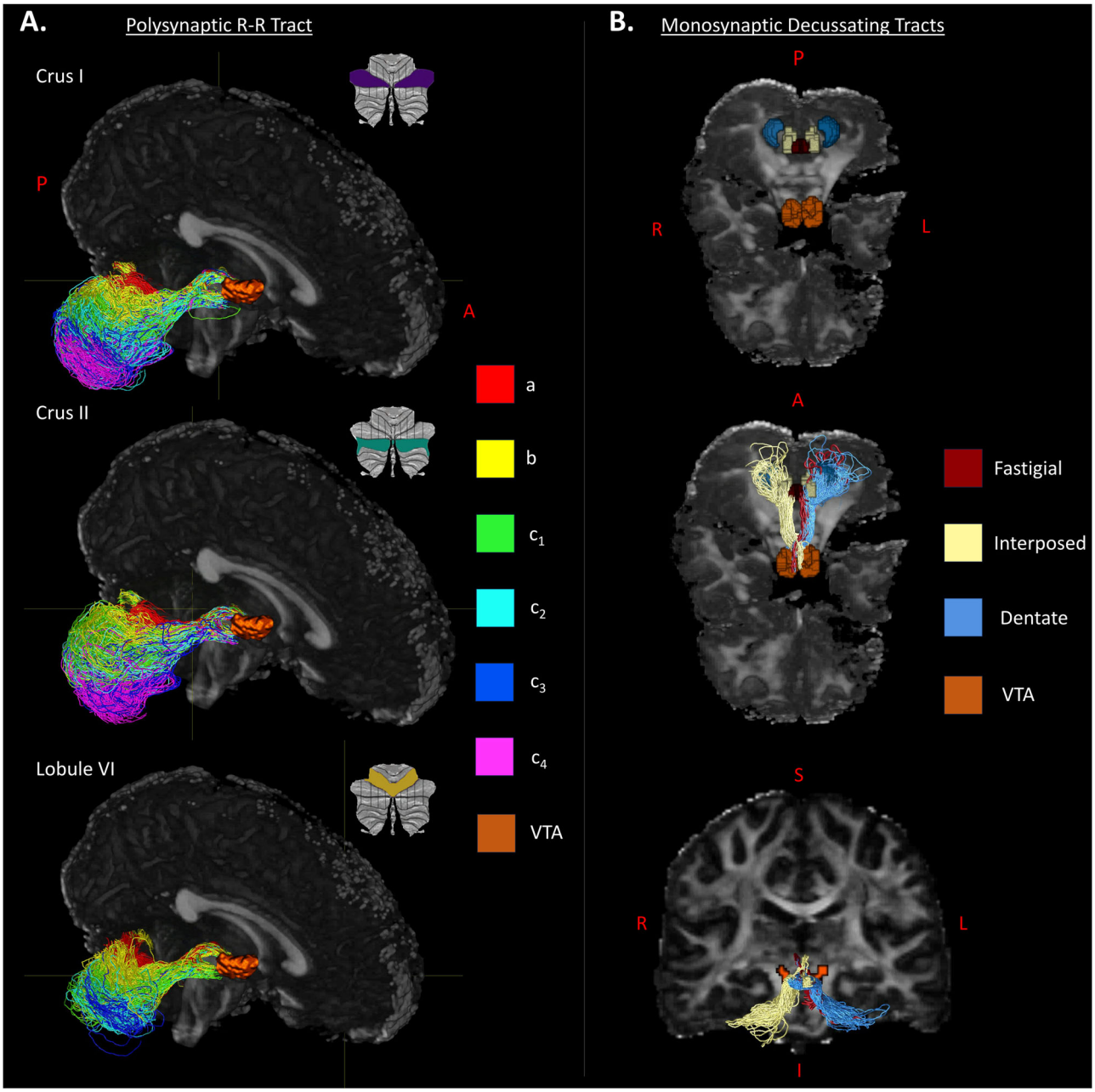

Figure 2. Tractography results showing connections between the cerebellar cortex in a representative subject, deep cerebellar nuclei, and VTA overlaid on the FA image. ***A***, Right hemisphere ipsilaterally traveling polysynaptic tracts are shown for sagittal segments (a, b, and c_1–c_4) within each cerebellar lobule. ***B***, Anatomical regions of interest (ROIs) include the three deep cerebellar nuclei (fastigial, interposed, and dentate) and the VTA. Tractography results of the monosynaptic tracts between the deep cerebellar nuclei and VTA, color-coded by the nuclei from which they were seeded.

synapsed onto the left or right VTA); (3) sagittal segment; and (4) lobule-by-sagittal segment interactions.

A false discovery rate (FDR) correction for multiple comparisons was applied to individual difference analyses. We used the FDR method since we expected these effects to be smaller than those observed in the anatomical analyses and did not want to be unduly strict. Further, we performed the correction separately for poly- and monosynaptic tracts (i.e., vectorizing the *p*-values for correction based on the type of tractography under study). Thus, in the case of polysynaptic tracts, the correction was performed by vectorizing four *p*-values within each ASR and NEO-FFI subscale separately. For monosynaptic tractographies, only three *p*-values were vectorized. In this way, we control for the number of tracts under study for any given analysis, based on tractography type. Importantly, this correction was only performed for correlations between self-report and microstructure averaged across all 100 nodes for each tract. The FDR correction was not performed on the quarter-wise analyses, as this was purely exploratory and meant to elucidate the driving force between the effects observed in the former analyses.

Finally, to check for the robustness of these relations, we performed ordinary least squares (OLS) regressions with robust standard errors to account for potential violations in the assumption of the independence of observations due to genetic relatedness within our sample. To do this, we used the *lm_robust()* command from the *estimatr* package in R, designating sibling status based on the HCP family IDs using the *cluster* argument.

Results

Due to the large number of analyses in the current report, a narrative summary of the statistical results is provided below. To view detailed information on raw streamline analyses, including Bonferroni-corrected *p*-values, bootstrapped confidence intervals, effect sizes, and effect size magnitude summaries, please refer to Tables 3 and 4. For the success rate of all tractography reconstructions, please see Extended Data Table 3-1. Note

Table 3. Anatomical main effects for poly- and monosynaptic tracts

									95% CI		
Measure 1	Measure 2	*n* 1	*n* 2	*W*	*p*	$p_{Bonferroni}$		Eff. Size (*r*)	Lower	Upper	Magnitude
Polysynaptic tractography main effects											
Direction											
R–R	L–L	92	80	551	2.37×10^{-6}	1.42×10^{-5}	****	0.54	0.37	0.70	Large
	R–L			33	4.10×10^{-14}	2.46×10^{-13}		0.85	0.82	0.87	
	L–R		32								
L–L	R–L	80	80	2,318	2.58×10^{-9}	1.55×10^{-8}	****	0.71	0.57	0.81	Large
	L–R		32	527	9.31×10^{-10}	5.59×10^{-9}		0.87	0.85	0.87	
R–L				50	2.82×10^{-5}	1.69×10^{-4}	***	0.70	0.48	0.85	
Lobule											
Crus I	Crus II	49	56	508	0.322	0.966	ns	0.16	0.007	0.44	Small
	Lobule VI		43	391	0.219	0.657		0.21	0.01	0.52	
Crus II		56		361	0.669	>0.999		0.07	0.005	0.41	
Segment											
a	b	77	83	1,851.5	1.00×10^{-3}	1.50×10^{-2}	*	0.39	0.18	0.58	Moderate
	c_1		75	562	4.00×10^{-3}	5.60×10^{-2}	†	0.37	0.12	0.60	
	c_2		62	217.5	8.70×10^{-5}	1.00×10^{-3}	**	0.56	0.33	0.75	Large
	c_3		48	27	1.83×10^{-8}	2.74×10^{-7}	****	0.80	0.66	0.87	
	c_4		56	8	5.68×10^{-12}	8.52×10^{-11}		0.86	0.81	0.87	
b	c_1	83	75	2,443	1.93×10^{-9}	2.90×10^{-8}		0.70	0.56	0.82	
	c_2		62	1,701	7.49×10^{-10}	1.12×10^{-8}		0.80	0.71	0.86	
	c_3		48	1,125	7.11×10^{-14}	1.07×10^{-12}		0.87	0.85	0.87	
	c_4		56	1,431	2.46×10^{-10}	3.69×10^{-9}		0.87	0.87	0.87	
c_1	c_2	75	62	1,669.5	3.27×10^{-9}	4.90×10^{-8}		0.77	0.66	0.84	
	c_3		48	1,128	1.42×10^{-14}	2.13×10^{-13}		0.87	0.87	0.87	
	c_4		56	1,485	1.67×10^{-10}	2.50×10^{-9}					
c_2	c_3	62	48	990	1.14×10^{-13}	1.71×10^{-12}					
	c_4		56	1,125	1.14×10^{-9}	1.71×10^{-8}					
c_3		48		946	2.27×10^{-13}	3.40×10^{-12}					
Monosynaptic tractography main effects											
Direction											
R–R	L–L	101	100	4,106	5.50×10^{-8}	3.30×10^{-7}	****	0.54	0.39	0.68	Large
	R–L		101	5,080	2.20×10^{-17}	1.32×10^{-16}		0.84	0.81	0.86	
	L–R		93	4,371	5.66×10^{-17}	3.40×10^{-16}		0.87	0.87	0.87	
L–L	R–L	100	101	4,606	8.46×10^{-13}	5.08×10^{-12}		0.72	0.61	0.80	
	L–R		93	4,371	5.66×10^{-17}	3.40×10^{-16}		0.87	0.87	0.87	
R–L		101		4,075	4.56×10^{-13}	2.74×10^{-12}		0.75	0.65	0.83	
Deep cerebellar nuclei											
FN	IN	97	99	550	5.02×10^{-11}	1.51×10^{-10}	****	0.67	0.55	0.77	Large
	DN		94	2,934	1.30×10^{-2}	3.90×10^{-2}	*	0.26	0.05	0.46	Small
IN		99		3,943	1.67×10^{-11}	5.01×10^{-11}	****	0.70	0.57	0.81	Large

Nonparametric pairwise comparisons using Wilcoxon signed-rank test investigating streamline count differences based on tract direction, lobule, segment, and deep nucleus. All confidence intervals were bootstrapped with 10,000 iterations. Success rates for all tractographies are reported in Table 3-1. Changes in results when controlling for tract length and waypoint volume are depicted in Tables 3-2 and 3-3. Directions are coded as follows: R–R, right to right (unilateral tract); L–L, left to left (unilateral tract); R–L, right to left (decussating tract); L–R, left to right (decussating tract). Note that in direction codes, the letter to the left of the hyphen represents the cerebellar hemisphere in which the tractography was seeded, while the letter right of the hyphen represents the VTA where it was terminated. Segments are coded as follows: a = vermis, b = paravermis; c_1–c_4 = neocerebellum, with higher numbers indicating more lateral segments. FN, fastigial nucleus; IN, interposed nucleus; DN, dentate nucleus. Further, *n* 1, the number of subjects included in the analyses for Measure 1, *n* 2, the number of subjects included in the analyses for Measure 2, and *W*, Wilcoxon test statistic. These subjects include those for whom nonzero "successful" reconstructions were achieved. Significance flags: †$p < 0.10$, *$p < 0.05$, **$p < 0.01$, ***$p < 0.001$, ****$p < 0.0001$.

Table 4. Polysynaptic anatomical interactions

Measure 1	Measure 2	*n* 1	*n* 2	*W*	*p*	$p_{bonferroni}$		Eff. Size (*r*)	CI 95% Lower	CI 95% Upper	Magnitude
Direction × Lobule											
Crus I											
R–R	L–L	97	87	3,131	1.97×10^{-9}	1.18×10^{-8}	****	0.65	0.51	0.77	Large
	R–L		90	3,953	1.49×10^{-15}	8.94×10^{-15}		0.85	0.81	0.86	
	L–R		52	1,326	5.30×10^{-10}	3.18×10^{-9}		0.87	0.87	0.87	
L–L	R–L	87	90	2,818.5	5.04×10^{-8}	3.02×10^{-7}		0.61	0.45	0.73	
	L–R		52	1,325	5.63×10^{-10}	3.38×10^{-9}		0.87	0.86	0.87	
R–L		90	52	1,235.5	8.25×10^{-8}	4.95×10^{-7}		0.75	0.61	0.85	
Crus II											
R–R	L–L	99	90	3,181	5.14×10^{-6}	3.08×10^{-5}	****	0.48	0.30	0.64	Moderate
	R–L		88	3,856	2.90×10^{-15}	1.74×10^{-14}		0.84	0.80	0.86	Large
	L–R		60	1,829	1.76×10^{-11}	1.06×10^{-10}		0.87	0.86	0.87	
L–L	R–L	90	88	3,019.5	1.12×10^{-9}	6.72×10^{-9}		0.67	0.55	0.78	
	L–R		60	1,828	1.85×10^{-11}	1.11×10^{-10}		0.87	0.86	0.87	
R–L		88		1,451	1.02×10^{-7}	6.12×10^{-7}		0.71	0.55	0.83	
Lobule VI											
R–R	L–L	95	86	2,581.5	3.85×10^{-4}	2.00×10^{-3}	**	0.39	0.19	0.57	Moderate
	R–L		88	3,873	1.64×10^{-15}	9.84×10^{-15}	****	0.85	0.82	0.86	Large
	L–R		45	990	1.14×10^{-13}	6.84×10^{-13}		0.87	0.87	0.87	
L–L	R–L	86	88	3,124	5.65×10^{-12}	3.39×10^{-11}		0.77	0.67	0.83	
	L–R		45	989	2.27×10^{-13}	1.36×10^{-12}		0.87	0.86	0.87	
R–L		88		810	1.63×10^{-5}	9.78×10^{-5}		0.62	0.40	0.78	
Direction × segment											
a											
R–R	L–L	100	97	3,695.5	5.87×10^{-7}	3.52×10^{-6}	****	0.51	0.34	0.66	Large
	R–L		98	4,652	2.70×10^{-16}	1.62×10^{-15}		0.83	0.79	0.86	
	L–R		78	3,002	2.61×10^{-14}	1.57×10^{-13}		0.87	0.87	0.87	
L–L	R–L	97	98	3,478	2.66×10^{-5}	1.60×10^{-4}	***	0.43	0.25	0.59	Moderate
	L–R		78	3,080	1.78×10^{-14}	1.07×10^{-13}	****	0.87	0.87	0.87	Large
R–L		98		2,701.5	7.46×10^{-9}	4.48×10^{-8}		0.65	0.51	0.78	
b											
R–R	L–L	101	100	3,637.5	1.32×10^{-4}	7.92×10^{-4}	***	0.38	0.20	0.55	Moderate
	R–L		98	4,763	1.22×10^{-16}	7.32×10^{-16}	****	0.84	0.80	0.86	Large
	L–R		85	3,655	1.19×10^{-15}	7.14×10^{-15}		0.87	0.87	0.87	
L–L	R–L	100	98	4,235.5	2.27×10^{-11}	1.36×10^{-10}		0.68	0.56	0.77	
	L–R	98	85	3,653	1.28×10^{-15}	7.68×10^{-15}		0.87	0.86	0.87	
R–L				3,144.5	2.01×10^{-10}	1.21×10^{-9}		0.70	0.57	0.80	
c_1											
R–R	L–L	99	94	3,345	8.96×10^{-6}	5.38×10^{-5}	****	0.46	0.28	0.63	Moderate
	R–L		96	4,615	6.51×10^{-17}	3.91×10^{-16}		0.85	0.83	0.87	Large
	L–R		76	2,926	3.68×10^{-14}	2.21×10^{-13}		0.87	0.87	0.87	
L–L	R–L	94	96	3,379	3.62×10^{-7}	2.17×10^{-6}		0.53	0.37	0.66	
	L–R	96	76	2,925	3.83×10^{-14}	2.30×10^{-13}		0.87	0.87	0.87	
R–L				2,594	8.19×10^{-11}	4.91×10^{-10}		0.75	0.64	0.84	
c_2											
R–R	L–L	99	91	3,348.5	3.69×10^{-8}	2.21×10^{-7}	****	0.58	0.42	0.72	Large
	R–L		92	4,236	3.25×10^{-16}	1.95×10^{-15}		0.85	0.82	0.87	
	L–R		64	2,079	3.79×10^{-12}	2.27×10^{-11}		0.87	0.86	0.87	
L–L	R–L	91	92	2,978.5	6.69×10^{-6}	4.01×10^{-5}		0.48	0.30	0.63	Moderate
	L–R		64	2,077	4.16×10^{-12}	2.50×10^{-11}		0.87	0.86	0.87	Large
R–L		92		1,823	3.00×10^{-9}	1.80×10^{-8}		0.75	0.62	0.85	
c_3											
R–R	L–L	98	87	3,072.5	2.30×10^{-7}	1.38×10^{-6}	****	0.56	0.38	0.71	Large
	R–L		91	4,059	5.89×10^{-16}	3.53×10^{-15}		0.85	0.83	0.87	
	L–R		50	1,224	1.22×10^{-9}	7.32×10^{-9}		0.87	0.86	0.87	
L–L	R–L	87	91	2,694	4.52×10^{-6}	2.71×10^{-5}		0.51	0.33	0.66	
	L–R		50	1,222	1.78×10^{-14}	1.07×10^{-13}		0.87	0.85	0.87	
R–L		91		1,100.5	1.24×10^{-6}	7.44×10^{-6}		0.69	0.51	0.83	
c_4											
R–R	L–L	97	88	2,580	9.84×10^{-4}	6.00×10^{-3}	**	0.36	0.16	0.54	moderate
	R–L			3,794.5	1.76×10^{-15}	1.06×10^{-14}	****	0.85	0.82	0.87	large
	L–R		59	1,705	4.92×10^{-11}	2.95×10^{-10}		0.86	0.84	0.87	
L–L	R–L	88	88	2,545	9.23×10^{-6}	5.54×10^{-5}		0.50	0.31	0.65	moderate

(*Table continues.*)

Table 4. Continued

Measure 1	Measure 2	*n* 1	*n* 2	*W*	*p*	$p_{bonferroni}$		Eff. Size (*r*)	CI 95% Lower	CI 95% Upper	Magnitude
	L–R		59	1,767	2.86×10^{-11}	1.72×10^{-10}		0.87	0.86	0.87	large
R–L				1,336.5	3.21×10^{-7}	1.93×10^{-6}		0.69	0.53	0.81	
Lobule × segment											
a											
Crus I	Crus II	80	90	491.5	4.97×10^{-7}	1.49×10^{-6}	****	0.57	0.40	0.73	Large
	Lobule VI	90	98	81	1.59×10^{-13}	4.77×10^{-13}		0.83	0.76	0.87	
Crus II				483.5	5.21×10^{-10}	1.56×10^{-9}		0.66	0.52	0.77	
b											
Crus I	Crus II	91	94	2,994	1.64×10^{-5}	4.92×10^{-5}	****	0.46	0.28	0.61	Moderate
	Lobule VI		89	2,744	5.98×10^{-5}	1.79×10^{-4}	***	0.44	0.24	0.61	
Crus II		94		1,749	6.02×10^{-1}	>0.999	ns	0.06	0.004	0.26	Small
c_1											
Crus I	Crus II	94	89	2,294.5	6.80×10^{-2}	2.05×10^{-1}	ns	0.20	0.02	0.39	Small
	Lobule VI		77	2,482.5	1.32×10^{-7}	3.96×10^{-7}	****	0.61	0.43	0.75	Large
Crus II		89		1,964.5	4.00×10^{-3}	1.30×10^{-2}	*	0.33	0.11	0.54	Moderate
c_2											
Crus I	Crus II	83	87	963	3.00×10^{-3}	8.00×10^{-3}	**	0.34	0.13	0.53	Moderate
	Lobule VI		64	2,016	5.29×10^{-12}	1.59×10^{-11}	****	0.87	0.87	0.87	Large
Crus II		87		1,952	8.15×10^{-12}	2.45×10^{-11}		0.87	0.86	0.87	
c_3											
Crus I	Crus II	77	77	530	3.09×10^{-5}	9.27×10^{-5}	****	0.50	0.31	0.67	Moderate
	Lobule VI		50	1,176	1.68×10^{-9}	5.04×10^{-9}		0.87	0.87	0.87	Large
Crus II				1,275	7.77×10^{-10}	2.33×10^{-9}		0.87	0.87	0.87	
c_4											
Crus I	Crus II	64	69	710	0.475	-	ns	0.10	0.006	0.36	Small

Nonparametric pairwise comparisons using the Wilcoxon signed-rank test investigating interactions between direction and lobule; direction and segment; and lobule and segment. All confidence intervals are bootstrapped using 10,000 iterations to yield stable estimates around the effect size. Changes in results when controlling for tract length and waypoint volume are depicted in Extended Data Tables 4-1 and 4-2, respectively. The orange area in the bottom panel overlaid on the tractography results represents the VTA. Note that R–R = tract originating in the right cerebellar and terminating in the ipsilateral VTA, L–L = tract originating in the left cerebellum and terminating in the ipsilateral VTA, R–L = tract originating in the right cerebellum and terminating in the contralateral VTA, and L–R = tract originating in the left cerebellum and terminating in the contralateral VTA. Further, $n = 1$ is the number of subjects included in the analyses for Measure 1, $n = 2$ is the number of subjects included in the analyses for Measure 2, and *W* represents the Wilcoxon test statistic. These subjects include those for whom nonzero "successful" reconstructions were achieved. Significance flags: $^{\dagger}p < 0.10$, $*p < 0.05$, $**p < 0.01$, $***p < 0.001$, $****p < 0.0001$.

that successful tractographies for the anatomical analyses were determined by the presence of nonzero reconstructions. Reconstructions that yielded values of 0 were not included in the analyses due to difficulty in adjudicating whether the failure to reconstruct was due to an error in the tracking algorithm or a true lack of fibers in a given subject. Finally, companion tables of length- and waypoint-corrected results for main effects and interactions can be found in Figure 3 *A,B* and the extended dataset [i.e., Extended Data Tables 3-2, 3-3 (main effects), 4-1, and 4-2 (interactions)]. In the following sections, we present findings from the cerebellar cortex to the VTA using the DCN as waypoints (polysynaptic tracts) and from the DCN to the VTA (monosynaptic tracts). Note that the use of the terms "main effect" and "interaction" are being used outside of the use of an analysis of variance: all analyses reported here are pairwise Wilcoxon signed-rank tests. We use the term "main effect" to describe comparisons when collapsing across certain anatomical dimensions (e.g., segment and lobule) and when considering them together (e.g., lobule and segment).

Anatomy findings

Main effects

Polysynaptic tracts. First, focused Wilcoxon signed-rank tests revealed a main effect of direction such that more streamlines travel between the cerebellar cortex and the ipsilateral VTA. All possible direction combinations were significantly different from one another. There was an effect of laterality (i.e., in which cerebellar hemisphere the tract originates) such that there was stronger connectivity from the right cerebellum to the VTA. This holds for both the ipsilaterally and contralaterally (e.g., decussating) traveling tracts. This effect persists after controlling for DCN volume and tract length.

Second, pairwise comparisons revealed no main effect of lobule. This finding held when controlling for average tract length. However, when controlling for DCN volume as a confound, we found a significant difference in connectivity between lobule VI and crus I, as well as a trending difference (after Bonferroni's correction) between lobule VI and crus II. Both effects are of moderate magnitude and suggest higher streamline density coming from lobule VI as compared with crus I/II.

Third, there is a main effect of "segment" such that nearly all segments significantly differ from one another. Pairwise comparisons between every segment revealed a higher number of streamlines coming from the paravermis (segment b) compared with the vermis proper. From there, there is a mediolateral gradient of decreasing connectivity. However, when controlling for average tract length as a potential confound, the difference between the vermis (a) and paravermis (b) becomes nonsignificant, and the difference between the vermis and c_1 becomes significant such that the vermis has more connectivity to the VTA overall, while all other comparisons remain effectively unchanged. Finally, after controlling for DCN volume, the difference in direction between the vermis (a) and paravermis (b) flips, such that the vermally seeded tracts contain higher streamline density traveling through the fastigial nucleus than does the paravermally seeded tracts travelling through the interposed nucleus. Moreover, when controlling for DCN size, the difference between the vermis and c_1 remains significant. All other findings remain

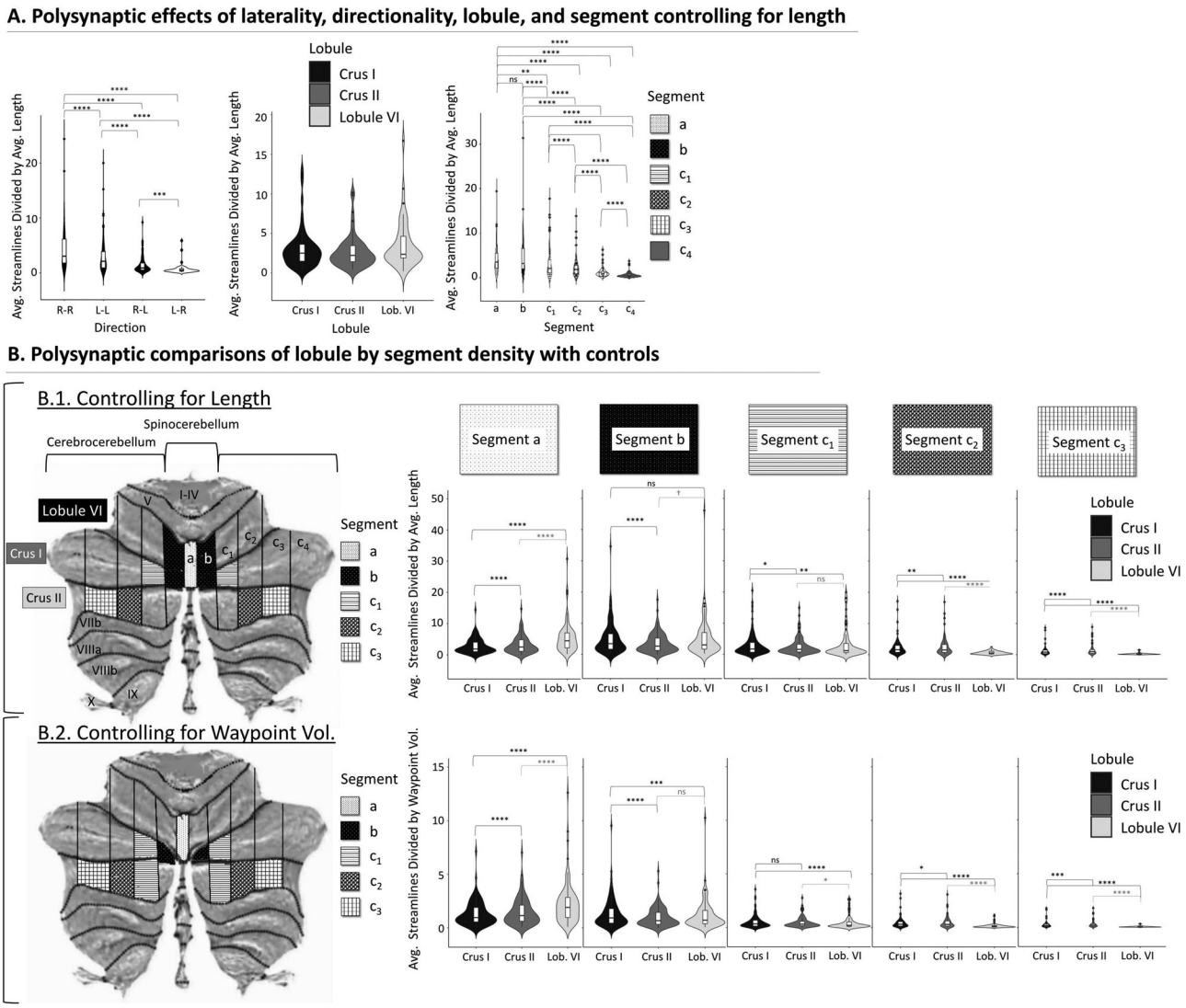

Figure 3. Illustrations of the main effect and interaction effect statistics with controls are not illustrated in Figure 4. ***A***, The statistical results of the main effects under study when controlling for average tract length. ***B***, The statical results of the segment by lobule interactions when controlling for average tract length (***B*.1.**) and waypoint volume (***B*.2.**). Note that the flat maps on the left in ***B*** contain pattern-coded highlights of which lobule contained the greatest streamline density within each segment when taking into account different controls. Note that for the flat map in ***B*.1.**, lobule VI and crus I are highlighted, as they both contained more connectivity than crus II, but did not differ from each other. Moreover, as in Figure 2*C*, no difference was found between crus I and II in segment c_4, and so it remains both unhighlighted in the flap map and unrepresented in the violin plots.

unchanged when controlling for DCN waypoint volume, meaning that the gradient of lessening connectivity with more laterally positioned segments endures.

Monosynaptic tracts. Focused Wilcoxon signed-rank tests revealed a main effect of direction such that more streamlines travel between the DCN and the ipsilateral VTA. All possible direction combinations were significantly different from one another. There was an effect of laterality such that there was stronger connectivity from the right DCN to the VTA. This holds for both the ipsilaterally and contralaterally (e.g., decussating) traveling tracts. This effect persists after controlling for tract length.

Second, there is a main effect of DCN. Pairwise comparisons revealed that most streamlines going to the VTA come from the interposed nucleus, second most from the fastigial, and the least coming from the dentate. This effect was not confounded by tract length.

All findings concerning the main effects are summarized in Figure 4.

Interactions

For the polysynaptic tractographies, there was neither an interaction between lobule and direction nor between segment and direction. That is to say that regardless of the lobule or segment that was seeded, the unilateral (i.e., ipsilaterally traveling) tract always contained more streamlines to the VTA than the contralaterally traveling or "decussating" tract, and the tract seeded in the right cerebellum always contained more VTA connectivity than those seeded in the left. These findings are robust and persist when controlling for both length and waypoint volume in the case of polysynaptic reconstructions.

There were, however, interactions between segment and lobule, such that different segments showed differing levels of connectivity between the three lobules under study. This is important because it provides insights into which lobule provides the most connectivity to the VTA within each segment. These findings are detailed below and in Figure 5. Findings for length and waypoint-controlled lobule-by-segment comparisons are summarized in Figure 3*B*.

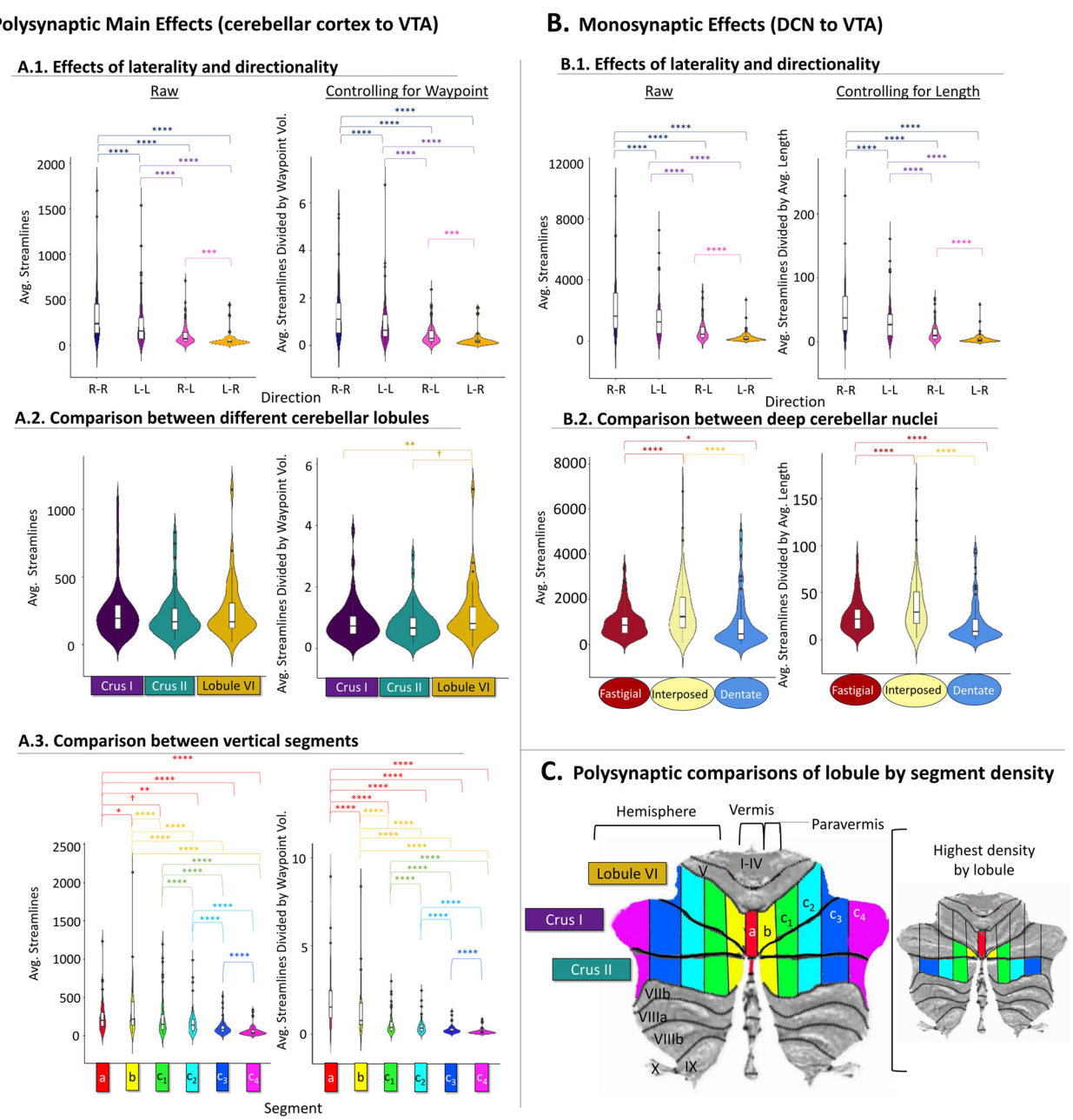

Figure 4. A summary of statistical results investigating gross pairwise comparisons. These are reported for both the polysynaptic (***A***) and monosynaptic (***B***) reconstructions. Each result is illustrated twice: on the left are the results using raw streamlines, and on the right are the streamline results when controlling for waypoint volume in voxels. Note that all plots are violin plots wherein dots outside the inner boxplot represent outliers. The results for the lobule-by-segment interactions are illustrated by cerebellar flat maps in section (***C***). The flat map on the left is meant to orient the viewer to the location of the cerebellar lobules and segments under study, while the flat map on the right has highlighted the lobule for each segment where streamline density was the highest. Note that segment c_1 is highlighted in crus I and II as both lobules contained more streamlines in this segment than lobule VI without being statistically different from each other. Also, segment c_4 contains no remaining highlights since the streamline count in crus I and II did not significantly differ from each other in this segment (this segment did not extend into lobule VI). How main effects and interactions change when controlling for tract length and waypoint volume are depicted in Figure 3. Note that R–R = tract originating in the right cerebellar and terminating in the ipsilateral VTA, L–L = tract originating in the left cerebellum and terminating in the ipsilateral VTA, R–L = tract originating in the right cerebellum and terminating in the contralateral VTA, and L–R = tract originating in the left cerebellum and terminating in the contralateral VTA. Significance flags: $^{\dagger}p < 0.10$, $*p < 0.05$, $**p < 0.01$, $***p < 0.001$.

Vermis (segment a). All possible lobule comparisons were significantly different from each other in the vermis, such that crus I vermal connectivity to the VTA contained the lowest connectivity, while lobule VI contained the most. This interaction holds after controlling for both average tract length and waypoint volume. This means that within the vermal regions under study, lobule VI contains the highest contribution of connections to the VTA, a finding that holds after holding multiple confounds constant.

Paravermis (segment b). There was a significant difference between paravermal connectivity to the VTA originating in crus I such that most of the connectivity from this segment originated in this lobule as compared with crus II and lobule VI. Furthermore,

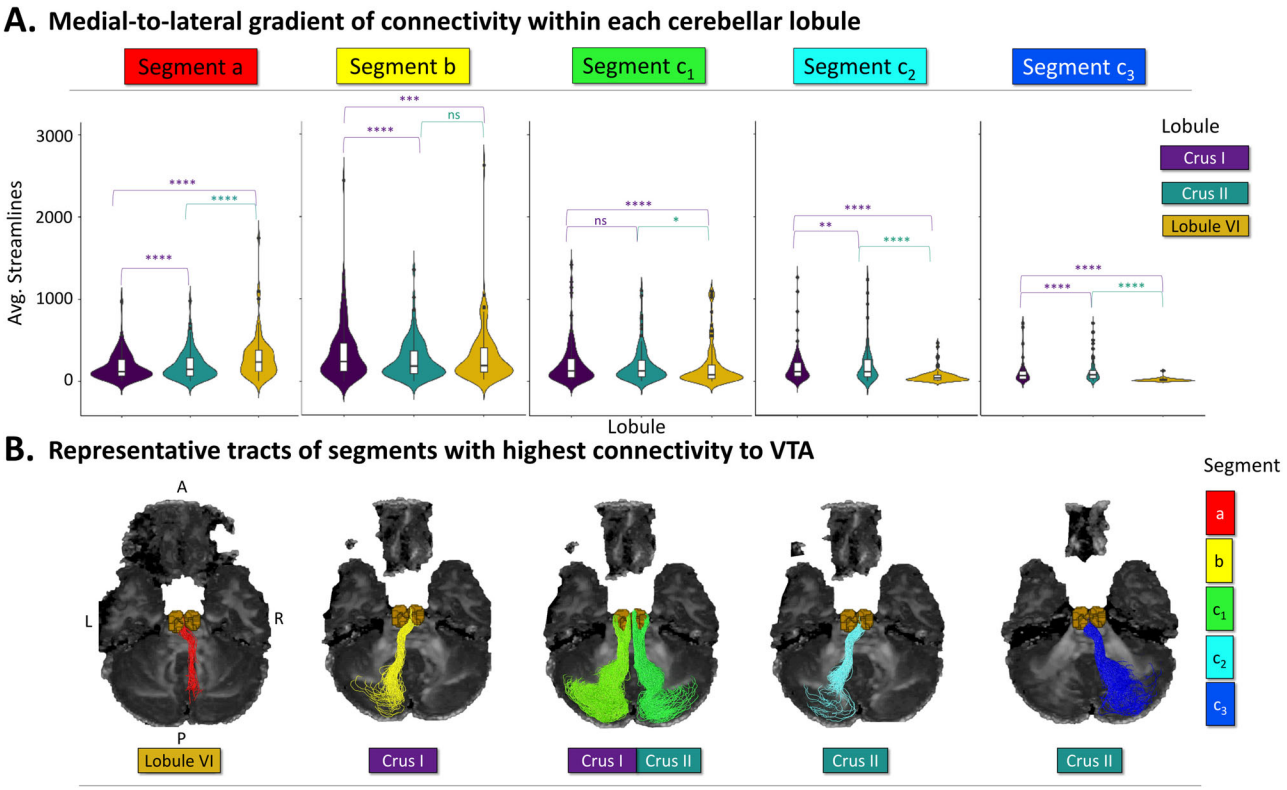

Figure 5. Topographical organization of cerebellum-VTA connectivity overlaid on FA image. ***A***, Medial segments of each cerebellar lobule have the highest connectivity with the VTA. ***B***, Representative tractography reconstructions for the segment of each cerebellar lobule with the highest connectivity to the VTA. Note that the laterality and directionality of the tracts are not meaningful but show instances of decussation in the polysynaptic reconstructions. Significance flags: $^{\dagger}p < 0.10$, $*p < 0.05$, $**p < 0.01$, $***p < 0.001$.

there was no difference between the relative amount of paravermal connectivity coming from crus II and lobule VI. This finding held when controlling for the volume of the DCN waypoints. However, when controlling for average streamline length, only crus I and crus II remained significantly different from one another, with this difference remaining in the same direction.

Cerebrocerebellum segment c_1. There was an interaction between lobule and segment in the case of c_1, such that lobule VI contains fewer VTA projections than both crus I and crus II while the latter two lobules remain nonsignificantly different from each other. This effect persists when controlling for waypoint volume. However, when controlling for length, it emerges that crus I contains more VTA connectivity than crus II and lobule VI, while the difference between crus II and lobule VI becomes nonsignificant.

Cerebrocerebellum segments c_2 and c_3. All possible lobule comparisons in segments c_2 and c_3 were significantly different from one another, such that crus II contains the most VTA connectivity in these segments, while lobule VI contains the least. These effects held after controlling for average tract length and waypoint volume within these segments.

Cerebrocerebellum segment c_4. There was no difference in segment c_4 between crus I/II, and one did not emerge when controlling for average tract length or waypoint volume.

Brain–behavior findings

Using the segments of the highest density identified in the anatomical investigation, we examined the relationship between tract microstructure and psychiatric self-report and personality factors. Robust correlations were revealed between all self-report measures and microstructure and in both the poly- and monosynaptic tracts.

For all brain self-report analyses, we further split the tracts into quarters, corresponding to the more superficial white matter (i.e., Q1) to deeper white matter (i.e., Q4). In the polysynaptic tract, Q1 corresponds to cerebellar fibers originating in the superficial layers of the cerebellar cortex and includes parallel fibers. Additionally, Q2 corresponds to the portion of the tract that converges on the DCN, while Q3 is the point of divergence away from the DCN, corresponding to the more inferior portion of the superior cerebellar peduncles. Finally, Q4 corresponds to the more superior portion of the superior cerebellar peduncle that innervates the ventral tegmental area. Note that the quarter-wise analysis was performed in order to assess which subsection of the tract under study was most responsible for driving the brain self-report effects. Note that the quarters in the monosynaptic analysis reflect a similar superficial-to-deep analysis of VTA-sending segments of the superior cerebellar peduncle.

Due to the large amount of data, statistics are reported only in the aforementioned tables but are summarized in narrative form below. We note that it may be of interest to some researchers to know how the cerebello-VTA tract originating in the left cerebellum contributes to social and affective functioning—a matter that is not discussed at length in the current study. Due to the issue of multiple comparisons, we restricted the brain self-report analyses to the right in an effort to reduce the proliferation of analyses. However, we note that upon cursory investigation of left-to-left cerebello-VTA microstructure, only revealed significant relations between overall average FA in segment c_1 crus II and ASR

somatic complaints and attention problems. While other trends emerged, these results were not as compelling as those in the right-to-right tract, whose investigation is compelled by a data-driven anatomical approach. Finally, while we preformed follow-up analyses using OLS regressions with robust standard errors to account for genetic relatedness within our sample, we do not describe these results in great detail below, as these checks for robustness did not affect the major findings of the current report or their interpretation. We refer readers to the extended dataset tables where these analyses can be found and note two major differences that did emerge in light of these analyses. First, when accounting for sibling status, the associations between tract FA and Agreeableness did not hold, especially within the quarter-wise analyses while controlling for relatedness and sex together. Further, controlling for sibling status altered the overall quarter-wise results such that Q1 had more instances of significance than Q2 for the polysynaptic tractographies. However, the finding that Q3 was the most frequent driver of effects and the finding that Q4 was never significant held in these analyses.

Correlations with Achenbach adult self-report

The findings for all ASR measures with FA across all 100 nodes of each polysynaptic tract under study are summarized in Figure 6 and Table 5, while the findings for the monosynaptic analytic counterparts are summarized in Figure 7 and Table 6. Note that the tables only delineate the exploratory results from the quarter-wise analysis. Descriptive statistics for the self-report measures and the tracts under study are summarized in Extended Data Tables 5-1 and 5-2. Furthermore, a complete correlation matrix with all self-report and neural measures is reported in Extended Data Table 5-3. Finally, how these associations are affected by accounting for genetic relatedness (i.e., "sibling status") within the sample, OLS regression results with robust standard errors are reported in Extended Data Table 6-1. This table provides results for both poly- and monosynaptic tractographies together.

In line with the growing emphasis on dimensional, rather than categorical, conceptualizations of psychopathology (e.g., Snyder et al., 2023), we not only examined anxiety and depression but also associations between tractography and a broad measure of internalizing symptoms. In this way, we sought to apply a Research Domain Criteria (RDoC) approach to assess levels of negative affective symptomology across multiple dimensions (Cuthbert and Insel, 2013). It is important to note that we had a priori hypotheses regarding certain ASR measures of interest (e.g., anxiety/depression, internalizing, and social withdrawal). However, we examined relations between all ASR subscales to get at a greater level of dissociability. These correlations are reported in Extended Data Table 5-3. It is important to note that the tracts under study in the current report are more associated with internalizing as opposed to externalizing symptoms (e.g., externalizing and aggression). Therefore, the subscales related to internalizing are discussed in greater detail below.

Anxiety and depression. Polysynaptic findings. Hypothesized correlations between the cerebello-VTA areas of highest tract density were identified between the vermal, paravermal, and cerebrocerebellar portions of the tract originating in crus II and anxiety and depression. All findings held when controlling for multiple comparisons. Quarter-wise analyses for polysynaptic tractographies revealed that Q3 emerged most often as driving this effect for each tract, followed by Q1 and Q2. Q4 never emerged as significant.

Monosynaptic findings. For the monosynaptic tractographies, correlations only emerged for the tracts originating in the fastigial and interposed nuclei (findings became trends after FDR correction). For the quarter-wise analyses, Q1 and Q2 were significant. Q3 and Q4 were never significant. All findings held when controlling for multiple comparisons.

Internalizing symptoms. Polysynaptic findings. Relations emerged between every polysynaptic tractography and internalizing symptoms, all of which survived FDR correction. The most frequently significant quarter was Q3, followed by Q2, and finally Q1. Q4 never emerged as significant.

Monosynaptic findings. There were significant relations between fastigial and interposed monosynaptic FA and internalizing symptoms, although they did not survive FDR correction. The only quarters implicated as driving these relations were Q1 and Q2.

Social withdrawal. Polysynaptic findings. When averaging across all 100 nodes, the only relations between social withdrawal and tract microstructure were with the cerebrocerebellar tracts originating in both crus I/II. Although these findings did not survive FDR correction, bootstrapped confidence intervals converged on significance for these tracts. The quarter that arose as most frequently driving the association was Q1, followed by Q2, and finally Q3. Q4 was never significant.

Monosynaptic findings. No tracts were significantly related to social withdrawal.

Somatic complaints. Polysynaptic findings. Somatic symptoms include a range of physical symptoms such as pain, dizziness, or shortness of breath. Somatic symptoms are distinct from but related to anxiety and depressive symptoms (Kong et al., 2022). Robust correlations between spinocerebellar segments of the cerebello-VTA tract and somatic complaints were found. For the cerebrocerebellar portions of the tract, only the portion originating in crus II showed a significant relation. All findings survived multiple comparisons corrections, and all significant tracts showed Q1–3 as equally driving the associations. Q4 was never as significant.

Monosynaptic findings. For the monosynaptic tractographies, only the fastigial and interposed showed significant relations with somatic complaints; both Q1 and Q2 were shown to drive this effect.

Attention problems. Polysynaptic findings. ASR attention problems were associated with lobule VI vermis–originating and crus II c_1–originating FA. Although these associations did not hold after FDR correction ($p_{FDR} = 0.050$ † in both cases), neither of the bootstrapped confidence intervals for these associations contained zero, bolstering the effects' robustness. In terms of which portion of the tracts drove this effect, Q1–3 are significant. It is important to note that Q2–3 are significant an equal number of times, while Q1 arises as significant only once.

Monosynaptic findings. No tracts emerged as significant.

Correlations with NEO five-factor inventory

Correlations between whole tract FA for the spino- and cerebrocerebellar tract segments are reported in the complete correlation matrix in Extended Data Table 5-4. As expected, there was no significant association between cerebellum-VTA FA and the personality traits of conscientiousness and extroversion. However,

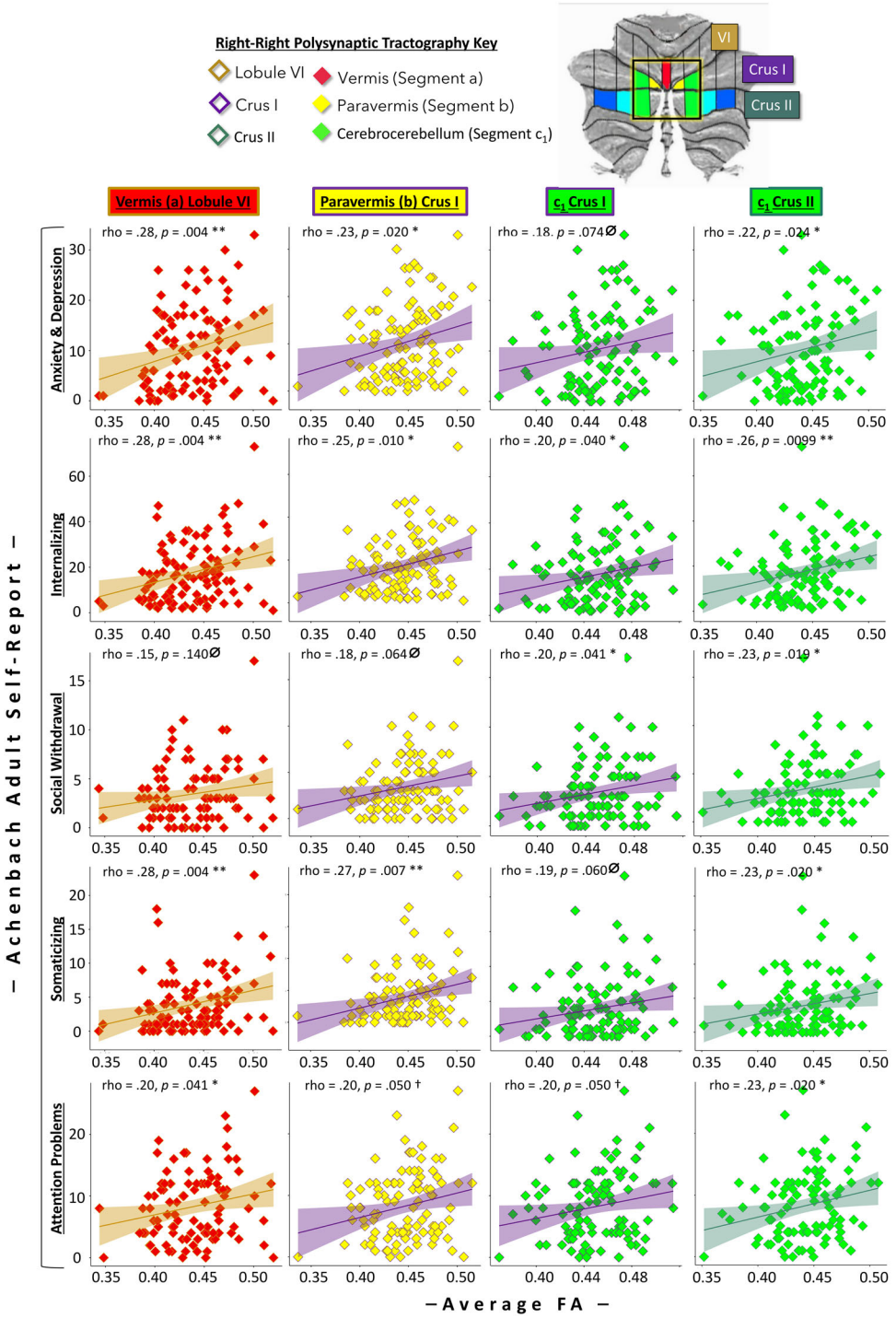

Figure 6. Summary of correlations between subscales on the ASR and FA averaged across all 100 nodes of the right-to-right traveling polysynaptic tracts of highest streamline density. Note that the *p*-values reflected here are not controlled for multiple comparisons. Correlations between ASR scores and FA in monosynaptic tracts are illustrated in Figure 7. Note that in the scatterplots, the lines represent trendlines illustrating the slope of the relation, and the shaded area around each trend line represents confidence bands. Confidence bands visualize sampling error around each slope. Significance flags: $^{\varnothing}p > 0.05$, $^{\dagger}p = 0.05$, $*p < 0.05$, $**p < 0.01$.

we did find associations between FA and neuroticism and agreeableness. Hence, these relations are expounded upon in further detail below.

Unlike the analyses above, subjects were not matched on the NEO-FFI by biological sex. Consequently, we identified sex differences in neuroticism, with females exhibiting higher levels of each trait [$W = 1{,}592$, $p = 0.031$ *, rrb = 0.25, 95% CI (0.03, 0.45) and a trend in agreeableness $W = 1{,}542$, $p = 0.069$ †, rrb = 0.21, 95% CI (−0.01, 0.41)]. To account for this in the following analyses, we report simple bivariate Spearman correlations and partial Spearman correlations accounting for sex. In each case, it is noted how controlling for sex changed the results. Complete FA-average correlations (e.g., FA collapsed across all 100 nodes for each tract) and quarter-wise results for poly- and monosynaptic tracts are reported in Table 7. How these associations are affected by accounting for genetic relatedness

Table 5. Polysynaptic associations with microstructure and psychiatric symptoms

Segment	Lobule	Section	Rho (ρ)	p-value		p-value FDR		95% CI: lower, upper
Fractional anisotropy correlations: ASR anxiety and depression								
a:vermis	VI	Avg.	0.28	0.004	**	0.016	**	(0.09, 0.46)
		Q1	0.23	0.023	*			
		Q2	0.24	0.017	*			
		Q3	0.24	0.014	*			
		Q4	0.09	0.362	ns			
b:paravermis	Crus I	Avg.	0.23	0.020	*	0.032	*	(0.03, 0.42)
		Q1	0.12	0.235	ns			
		Q2	0.21	0.034	*			
		Q3	0.23	0.020	*			
		Q4	0.09	0.391	ns			
c_1:cerebrocerebellum		Avg.	0.18	0.074	†	0.074	†	(−0.02, 0.37)
		Q1	0.05	0.647	ns			
		Q2	0.06	0.545	ns			
		Q3	0.20	0.044	*			
		Q4	0.09	0.379	ns			
	Crus II	Avg.	0.22	0.024	*	0.032	*	(0.03, 0.40)
		Q1	0.23	0.022	*			
		Q2	0.11	0.260	ns			
		Q3	0.22	0.026	*			
		Q4	0.06	0.523	ns			
Fractional anisotropy correlations: ASR internalizing symptoms								
a:vermis	VI	Avg.	0.28	0.004	**	0.013	*	(0.08, 0.47)
		Q1	0.26	0.010	*			
		Q2	0.26	0.009	**			
		Q3	0.23	0.020	*			
		Q4	0.06	0.541	ns			
b:paravermis	Crus I	Avg.	0.26	0.010	*	0.013	*	(0.05, 0.44)
		Q1	0.19	0.058	†			
		Q2	0.24	0.018	*			
		Q3	0.24	0.014	*			
		Q4	0.07	0.462	ns			
c_1:cerebrocerebellum		Avg.	0.21	0.040	*	0.040	*	(0.01, 0.39)
		Q1	0.11	0.279	ns			
		Q2	0.12	0.247	ns			
		Q3	0.20	0.041	*			
		Q4	0.07	0.470	ns			
	Crus II	Avg.	0.26	0.010	*	0.013	*	(0.06, 0.43)
		Q1	0.27	0.007	*			
		Q2	0.20	0.046	*			
		Q3	0.24	0.014	*			
		Q4	0.06	0.561	ns			
Fractional anisotropy correlations: ASR social withdrawal								
a:vermis	VI	Avg.	0.15	0.142	ns	0.142	ns	(−0.04, 0.33)
		Q1	0.25	0.011	*			
		Q2	0.15	0.137	ns			
		Q3	0.07	0.484	ns			
		Q4	−0.02	0.819	ns			
b:paravermis	Crus I	Avg.	0.19	0.064	†	0.085	†	(−0.02, 0.38)
		Q1	0.27	0.007	**			
		Q2	0.21	0.040	*			
		Q3	0.16	0.120	ns			
		Q4	0.01	0.908	ns			
c_1:cerebrocerebellum		Avg.	0.20	0.041	*	0.082	†	(0.01, 0.39)
		Q1	0.20	0.046	*			
		Q2	0.17	0.085	†			
		Q3	0.17	0.091	†			
		Q4	0.04	0.663	ns			
	Crus II	Avg.	0.23	0.019	*	0.076	†	(0.04, 0.41)
		Q1	0.21	0.032	*			
		Q2	0.30	0.003	**			
		Q3	0.21	0.033	*			
		Q4	0.03	0.737	ns			

(*Table continues.*)

Table 5. Continued

Segment	Lobule	Section	Rho (ρ)	p-value		p-value FDR		95% CI: lower, upper
Fractional anisotropy correlations: ASR somaticizing symptoms								
a:vermis	VI	Avg.	0.28	0.004	**	0.014	*	(0.08, 0.48)
		Q1	0.29	0.003	**			
		Q2	0.33	<0.001	***			
		Q3	0.23	0.023	*			
		Q4	0.02	0.878	ns			
b:paravermis	Crus I	Avg.	0.27	0.007	**	0.014	*	(0.07, 0.45)
		Q1	0.22	0.027	*			
		Q2	0.26	0.010	**			
		Q3	0.24	0.016	*			
		Q4	0.03	0.805	ns			
c_1:cerebrocerebellum		Avg.	0.19	0.060	†	0.060	†	(−0.02, 0.38)
		Q1	0.16	0.110	ns			
		Q2	−0.08	0.199	ns			
		Q3	0.17	0.090	†			
		Q4	0.02	0.830	ns			
	Crus II	Avg.	0.23	0.020	*	0.027	*	(0.05, 0.41)
		Q1	0.27	0.006	**			
		Q2	0.22	0.031	*			
		Q3	0.21	0.032	*			
		Q4	0.04	0.702	ns			
Fractional anisotropy correlations: ASR attention problems								
a:vermis	VI	Avg.	0.20	0.041	*	0.050 †		(0.01, 0.39)
		Q1	0.10	0.317	ns			
		Q2	0.25	0.014	*			
		Q3	0.15	0.135	ns			
		Q4	0.03	0.784	ns			
b:paravermis	Crus I	Avg.	0.20	0.050	†	0.050	†	(−0.004, 0.37)
		Q1	0.12	0.247	ns			
		Q2	0.18	0.079	†			
		Q3	0.21	0.038	*			
		Q4	0.06	0.536	ns			
c_1:cerebrocerebellum		Avg.	0.20	0.050	†	0.050	†	(0.002, 0.38)
		Q1	0.16	0.108	ns			
		Q2	0.12	0.221	ns			
		Q3	0.18	0.081	†			
		Q4	0.06	0.567	ns			
	Crus II	Avg.	0.23	0.020	*	0.050	†	(0.05, 0.40)
		Q1	0.29	0.003	**			
		Q2	0.20	0.042	*			
		Q3	0.20	0.044	*			
		Q4	0.06	0.540	ns			

Correlations with Achenbach Self-Report (ASR) subscales and fractional anisotropy (FA) values for the right-to-right traveling polysynaptic tracts with the highest densities. A double dissociation between spinocerebellum (i.e., vermis and paravermis sending projections through the fastigial and interposed nuclei, respectively) and cerebrocerebellum (i.e., lateral cortical regions sending projections through the dentate) on somaticizing symptoms and social withdrawal, respectively. The N for all correlations is 101, the degrees of freedom for all tests is 99, and all confidence intervals are bootstrapped using 10,000 iterations. False discovery rate (FDR) correction for multiple comparisons was performed for the number of tracts within the polysynaptic (4 tracts). We used the FDR method to control for multiple comparisons, as we anticipated the effects to be smaller than those in the anatomy analyses and did not want to be unduly strict. Moreover, we chose to look at self-report measures for which we had a priori hypotheses, further warranting a less stringent approach to significance testing. Bootstrapped confidence intervals to further check for robustness of effects. Extended data supporting the findings here are reported in Extended Data Tables 5-1 through 5-3. Significance flags: $^{\dagger}p < 0.10$, $*p < 0.05$, $**p < 0.01$, $***p < 0.001$.

(i.e., "sibling status") within the sample, OLS regression results with robust standard errors are reported in Extended Data Table 7-1. This table provides results for both poly- and monosynaptic tractographies together. Moreover, this table describes how results change when looking at genetic relatedness together with sex. Further, a numeric heatmap summarizing the number of times each quarter was implicated as driving the effects across all poly- versus monosynaptic associations is depicted in Table 8, and how this map changes when accounting for sibling status is summarized in Extended Data Table 8-1.

Neuroticism. Polysynaptic findings. All polysynaptic tractographies of the highest tract density correlated with NEO-FFI neuroticism, and all correlations survived FDR correction. Q3 was the most frequently significant quarter, followed by Q2, while neither Q1 nor Q4 were ever significant. When controlling for sex, the correlations with overall tract FA held and survived FDR correction. However, the only remaining quarters that reached significance are Q3 and Q2, each to a lesser extent than previously.

Monosynaptic findings. For the monosynaptic tractographies, only the fastigial and interposed tracts correlated with neuroticism, which survived FDR correction. Q1 and Q2 were significant. Neither Q3 nor Q4 were ever significant.

Agreeableness. Polysynaptic findings. Lobule VI vermis–originating FA significantly correlated with agreeableness. This finding did not survive FDR correction, although the bootstrapped confidence interval suggested a degree of robustness

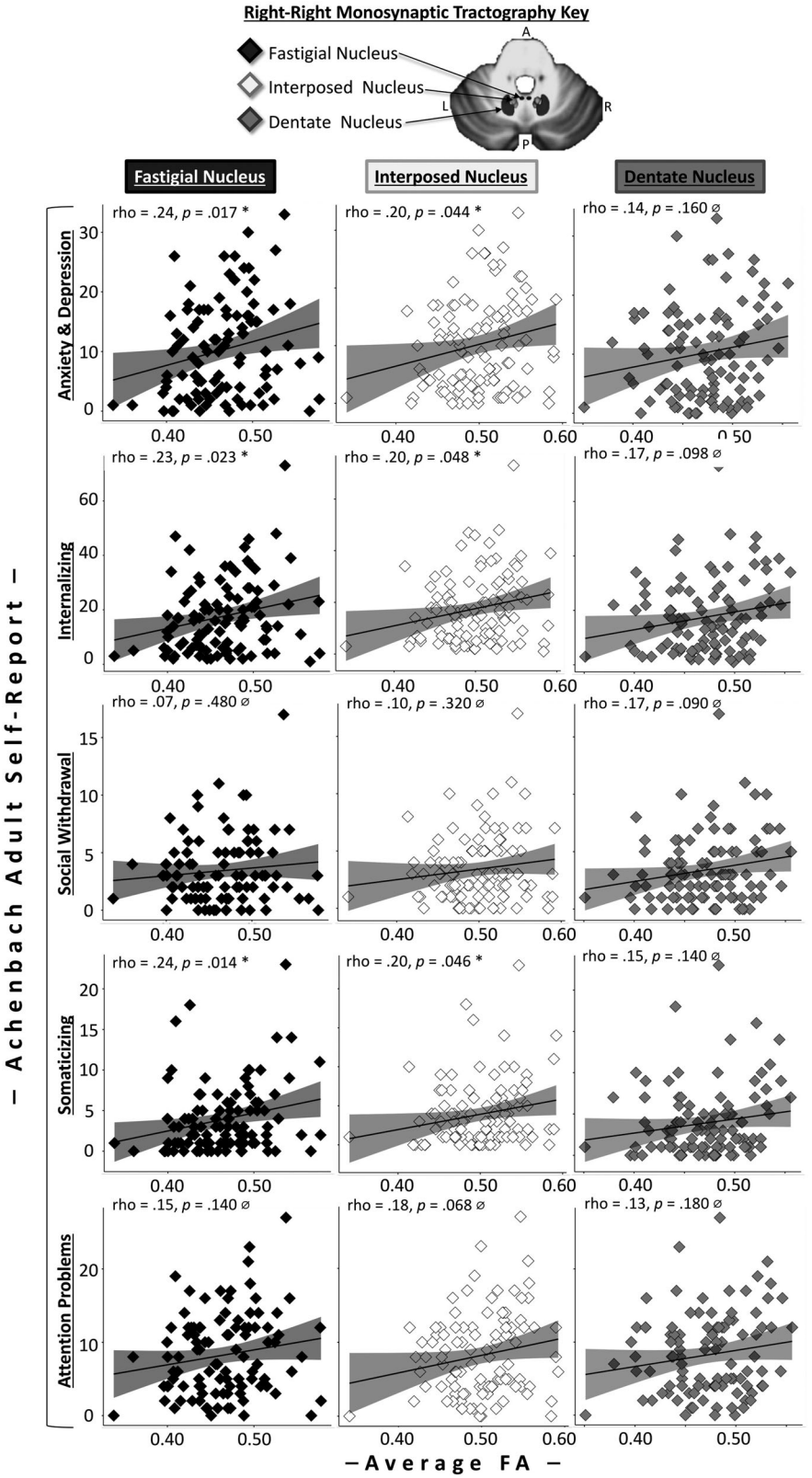

Figure 7. The results between monosynaptic tractography FA for each deep cerebellar nucleus traveling right-to-right and ASR measures. Note that FA is averaged across all 100 nodes for each tract, and the *p*-values are not corrected for multiple comparisons. Significance flags: $^{\varnothing}p > 0.05$, $^{*}p < 0.05$, $^{**}p < 0.01$.

in the effect, as it did not contain 0. Although the vermal tract was the only one overall to reach significance, Q3 was significantly related to agreeableness in all four polysynaptic tracts. These findings held when controlling for sex. The only change was that the relation between Q3 FA and agreeableness for the crus II c_1 tract became a trend.

Monosynaptic findings. For the monosynaptic tractographies, all tracts were significantly related to agreeableness. For the tracts

Table 6. Monosynaptic relations between microstructure and psychiatric symptoms

Deep cerebellar nucleus	Section	Rho (ρ)	p-value		p-value FDR		95% CI: lower, upper
Fractional anisotropy correlations: ASR anxiety and depression							
Fastigial	Avg.	0.24	0.017	*	0.051	†	(0.03, 0.42)
	Q1	0.16	0.107	ns			
	Q2	0.25	0.011	*			
	Q3	0.17	0.096	†			
	Q4	0.03	0.778	ns			
Interposed	Avg.	0.20	0.044	*	0.066	†	(0.01, 0.38)
	Q1	0.20	0.044	*			
	Q2	0.22	0.030	*			
	Q3	0.13	0.204	ns			
	Q4	0.05	0.606	ns			
Dentate	Avg.	0.14	0.159	ns	0.159	†	(−0.07, 0.33)
	Q1	0.04	0.707	ns			
	Q2	0.12	0.231	ns			
	Q3	0.14	0.166	ns			
	Q4	0.09	0.348	ns			
Fractional anisotropy correlations: ASR internalizing symptoms							
Fastigial	Avg.	0.23	0.023	*	0.069	†	(0.02, 0.42)
	Q1	0.16	0.110	ns			
	Q2	0.26	0.010	*			
	Q3	0.14	0.155	ns			
	Q4	0.01	0.908	ns			
Interposed	Avg.	0.20	0.048	*	0.072	†	(0.001, 0.38)
	Q1	0.20	0.045	*			
	Q2	0.22	0.026	*			
	Q3	0.13	0.200	ns			
	Q4	0.04	0.696	ns			
Dentate	Avg.	0.17	0.098	†	0.098	†	(−0.04, 0.35)
	Q1	0.12	0.240	ns			
	Q2	0.16	0.117	ns			
	Q3	0.15	0.147	ns			
	Q4	0.08	0.459	ns			
Fractional anisotropy correlations: ASR social withdrawal							
Fastigial	Avg.	0.07	0.481	ns	0.481	ns	(−0.12, 0.26)
	Q1	0.01	0.900	ns			
	Q2	0.11	0.256	ns			
	Q3	0.03	0.734	ns			
	Q4	−0.05	0.605	ns			
Interposed	Avg.	0.10; 0.325	0.325	ns	0.481	ns	(−0.09, 0.29)
	Q1	0.08; 0.439	0.439	ns			
	Q2	0.11; 0.261	0.261	ns			
	Q3	0.08; 0.436	0.436	ns			
	Q4	0.001;0.996	0.996	ns			
Dentate	Avg.	0.17; 0.090	0.090	†	0.270	ns	(−0.04, 0.36)
	Q1	0.24; 0.018	0.018	*			
	Q2	0.15; 0.125	0.125	ns			
	Q3	0.11; 0.268	0.268	ns			
	Q4	0.05; 0.597	0.597	ns			
Fractional anisotropy correlations: ASR somaticizing symptoms							
Fastigial	Avg.	0.24; 0.014	0.014	*	0.042	*	(0.03, 0.45)
	Q1	0.26	0.008	**			
	Q2	0.26	0.008	**			
	Q3	0.10	0.344	ns			
	Q4	−0.01	0.918	ns			
Interposed	Avg.	0.20	0.046	*	0.069	†	(−0.01, 0.39)
	Q1	0.23	0.019	*			
	Q2	0.24	0.017	*			
	Q3	0.11	0.290	ns			
	Q4	−0.01	0.945	ns			
Dentate	Avg.	0.15	0.139	ns	0.139	ns	(−0.06, 0.35)
	Q1	0.15	0.143	ns			
	Q2	0.15	0.125	ns			
	Q3	0.14	0.164	ns			
	Q4	−0.01	0.940	ns			
Fractional anisotropy correlations: ASR attention problems							
Fastigial	Avg.	0.15	0.138	ns	0.181	ns	(−0.0, −0.33)
	Q1	0.10	0.310	ns			
	Q2	0.17	0.100	ns			
	Q3	0.09	0.376	ns			
	Q4	0.004	0.968	ns			
Interposed	Avg.	0.18	0.068	†	0.181	ns	(−0.01, 0.36)
	Q1	0.18	0.074	†			
	Q2	0.19	0.054	†			
	Q3	0.11	0.278	ns			
	Q4	0.01	0.946	ns			
Dentate	Avg.	0.13	0.181	ns	0.181	ns	(−0.07, 0.33)
	Q1	0.12	0.246	ns			
	Q2	0.09	0.358	ns			
	Q3	0.15	0.133	ns			
	Q4	0.05	0.652	ns			

Correlations with Achenbach Self-Report (ASR) subscales and fractional anisotropy (FA) values for the right-to-right traveling monosynaptic tracts with the highest densities. It is also reported which quarter is responsible for driving each effect. FDR corrections are performed only for associations between personality traits and tracts averaged across all 100 nodes resulting in a vector of 3 p-values per correction). In Extended Data Table 6-1, we check for robustness of results between both the poly- and monosynaptic tractography FA and ASR measures when accounting for genetic relatedness within the sample. The N for all correlations is 101, and the degrees of freedom for all tests is 99. Significance flags: $^{\dagger}p < 0.10$, $*p < 0.05$, $**p < 0.01$.

originating in the fastigial and interposed, both Q1 and Q2 were significant, whereas in the tract originating in the dentate, only Q3 was significant.

Discussion

Current findings

In this study, we charted the topographic organization of VTA-sending cerebellar projections. Further, we charted the relationship between FA and a priori indices of socioaffective functioning. We took an RDoC approach and assessed associations between tractography and broad measures of internalizing symptoms and negative affective symptomology. This revealed robust associations between FA in high-density portions of the cerebello-VTA tract and measures of psychiatric and personality self-report. Strikingly, we found that midline regions of the polysynaptic cerebello-VTA tract were uniquely associated with social withdrawal, while the monosynaptic fastigial and interposed tracts were uniquely associated with somatic complaints. Finally, we identified that the tract portion exiting the deep cerebellar nuclei was most responsible for driving the observed brain self-report effects (e.g., Q3), followed by Q2, and then Q1, representing the more superficial (i.e., closer to the cerebellar cortical surface) partitions of the cerebello-VTA tracts.

Anatomical findings

We found the highest density of streamlines in the cerebello-VTA tract was from the paravermis, and predictably, from the interposed nucleus of the DCN. The paravermis is known to calibrate motor control of the distal limbs (Unverdi and Alsayouri, 2023). Newer studies are slowly expanding the role of this region, beyond motor calibration. Paravermal lesions in mice result in downstream spikes in dopamine D1 receptor (DRD1) activity in the contralateral medial striatum and dopamine transporter attenuation in the dorsolateral striatum (Delis et al., 2013). The influence of the interposed nucleus and the paravermis on dopamine activity is echoed in a study by Snider

Table 7. Poly- and monosynaptic relations between microstructure and personality traits

									95% CI	
Type	Segment/DCN	Lobule	Section	Rho (ρ)	p-value		p-value FDR		Lower	Upper
A. Relations between personality factors and fractional anisotropy alone										
Big five-factor inventory neuroticism										
R–R Polysynaptic	a:vermis	VI	Avg.	0.28	0.005	**	0.012	*	0.07	0.46
			Q1	0.13	0.212	ns			−0.08	0.32
			Q2	0.21	0.032	*			0.01	0.40
			Q3	0.25	0.010	*			0.05	0.44
			Q4	0.14	0.171	ns			−0.07	0.33
	b:paravermis	Crus I	Avg.	0.27	0.006	**	0.012	*	0.08	0.45
			Q1	0.14	0.172	ns			−0.06	0.33
			Q2	0.29	0.004	**			0.09	0.46
			Q3	0.24	0.015	*			0.04	0.42
			Q4	0.13	0.189	ns			−0.08	0.33
	c_1:cerebro-cerebellum		Avg.	0.22	0.026	*	0.026	*	0.02	0.40
			Q1	0.04	0.712	ns			−0.16	0.25
			Q2	0.14	0.169	ns			−0.05	0.32
			Q3	0.21	0.039	*			0.01	0.39
			Q4	0.13	0.196	ns			−0.08	0.33
		Crus II	Avg.	0.25	0.012	*	0.016	*	0.05	0.43
			Q1	0.19	0.059	†			−0.004	0.37
			Q2	0.15	0.142	ns			−0.05	0.34
			Q3	0.21	0.040	*			0.01	0.39
			Q4	0.11	0.256	ns			−0.09	0.31
R–R Monosynaptic	Fastigial		Avg.	0.25	0.014	*	0.036	*	0.05	0.42
			Q1	0.15	0.141	ns			−0.06	0.34
			Q2	0.25	0.010	*			0.05	0.44
			Q3	0.18	0.065	†			−0.02	0.37
			Q4	0.08	0.432	ns			−0.13	0.28
	Interposed		Avg.	0.22	0.024	*	0.036	*	0.03	0.40
			Q1	0.22	0.031	*			0.02	0.39
			Q2	0.24	0.016	*			0.05	0.41
			Q3	0.13	0.186	ns			−0.07	0.32
			Q4	0.12	0.242	ns			−0.10	0.32
	Dentate		Avg.	0.18	0.074	†	0.074	†	−0.02	0.37
			Q1	0.05	0.615	ns			−0.15	0.24
			Q2	0.13	0.212	ns			−0.07	0.32
			Q3	0.15	0.129	ns			−0.04	0.34
			Q4	0.15	0.143	ns			−0.07	0.35
Big five-factor inventory agreeableness										
R–R Polysynaptic	a:vermis	VI	Avg.	0.24	0.017	*	0.068	†	0.05	0.41
			Q1	0.02	0.831	ns			−0.18	0.23
			Q2	0.16	0.118	ns			−0.04	0.35
			Q3	0.29	0.003	**			0.11	0.46
			Q4	0.17	0.084	†			−0.02	0.36
	b:paravermis	Crus I	Avg.	0.17	0.100	ns	0.100	ns	−0.03	0.34
			Q1	−0.10	0.341	ns			−0.30	0.11
			Q2	−0.02	0.838	ns			−0.22	0.19
			Q3	0.24	0.015	*			0.06	0.41
			Q4	0.14	0.156	ns			−0.05	0.33
	c_1:cerebro-cerebellum		Avg.	0.17	0.089	†	0.100	ns	−0.02	0.35
			Q1	−0.16	0.120	ns			−0.35	0.04
			Q2	0.04	0.707	ns			−0.17	0.24
			Q3	0.25	0.013	*			0.06	0.42
			Q4	0.13	0.185	ns			−0.06	0.32
		Crus II	Avg.	0.17	0.096	†	0.100	ns	−0.01	0.34
			Q1	0.01	0.951	ns			−0.22	0.22
			Q2	−0.05	0.608	ns			−0.25	0.15
			Q3	0.20	0.041	*			0.02	0.38
			Q4	0.12	0.242	ns			−0.08	0.30
R–R Monosynaptic	Fastigial		Avg.	0.27	0.006	**	0.015	*	0.09	0.44
			Q1	0.20	0.042	*			0.01	0.38
			Q2	0.29	0.004	**			0.10	0.45
			Q3	0.17	0.099	†			−0.03	0.35
			Q4	0.13	0.190	ns			−0.07	0.32

(*Table continues.*)

Table 7. Continued

Type	Segment/DCN	Lobule	Section	Rho (ρ)	p-value		p-value FDR		95% CI Lower	95% CI Upper
	Interposed		Avg.	0.26	0.010	**	0.015	*	0.08	0.42
			Q1	0.22	0.025	*			0.03	0.40
			Q2	0.26	0.008	**			0.07	0.44
			Q3	0.15	0.134	ns			−0.04	0.33
			Q4	0.10	0.323	ns			−0.10	0.29
	Dentate		Avg.	0.21	0.033	*	0.033	*	0.02	0.39
			Q1	0.04	0.728	ns			−0.17	0.24
			Q2	0.15	0.124	ns			−0.05	0.35
			Q3	0.24	0.018	*			0.05	0.41
			Q4	0.09	0.377	ns			−0.11	0.28
B. Partial correlations with fractional anisotropy, personality factors, and gender										
Big five-factor inventory neuroticism										
R–R Polysynaptic	a:vermis	VI	Avg.	0.24	0.017	*	0.041	*	0.03	0.43
			Q1	0.11	0.263	ns			−0.09	0.31
			Q2	0.18	0.071	†			−0.02	0.38
			Q3	0.22	0.031	*			0.004	0.41
			Q4	0.11	0.262	ns			−0.10	0.32
	b:paravermis	Crus I	Avg.	0.23	0.024	*	0.041	*	0.02	0.41
			Q1	0.12	0.223	ns			−0.08	0.33
			Q2	0.24	0.016	*			0.06	0.42
			Q3	0.19	0.053	†			−0.01	0.38
			Q4	0.12	0.226	ns			−0.09	0.32
	c_1:cerebro-cerebellum		Avg.	0.17	0.087	†	0.087	ns	−0.03	0.37
			Q1	0.02	0.841	ns			−0.17	0.22
			Q2	0.08	0.435	ns			−0.11	0.27
			Q3	0.16	0.110	ns			−0.03	0.36
			Q4	0.12	0.239	ns			−0.09	0.32
		Crus II	Avg.	0.22	0.031	*	0.041	*	0.03	0.40
			Q1	0.19	0.064	†			−0.01	0.38
			Q2	0.12	0.252	ns			−0.09	0.31
			Q3	0.17	0.095	†			−0.03	0.36
			Q4	0.10	0.325	ns			−0.11	0.30
R–R Monosynaptic	Fastigial		Avg.	0.21	0.037	*	0.094	†	0.01	0.40
			Q1	0.11	0.262	ns			−0.09	0.31
			Q2	0.21	0.032	*			0.02	0.41
			Q3	0.17	0.083	†			−0.03	0.37
			Q4	0.06	0.575	ns			−0.15	0.26
	Interposed		Avg.	0.19	0.063	†	0.094	†	0.003	0.37
			Q1	0.16	0.108	ns			−0.02	0.35
			Q2	0.20	0.051	†			0.01	0.38
			Q3	0.12	0.229	ns			−0.08	0.32
			Q4	0.10	0.333	ns			−0.11	0.31
	Dentate		Avg.	0.13	0.208	ns	0.208	ns	−0.07	0.32
			Q1	0.002	0.986	ns			−0.19	0.20
			Q2	0.07	0.472	ns			−0.13	0.27
			Q3	0.11	0.269	ns			−0.08	0.31
			Q4	0.14	0.163	ns			−0.07	0.35
Big five-factor inventory agreeableness										
R–R Polysynaptic	a:vermis	VI	Avg.	0.20	0.042	*	0.168	ns	0.02	0.38
			Q1	0.01	0.931	ns			−0.19	0.21
			Q2	0.13	0.210	ns			−0.08	0.32
			Q3	0.24	0.008	**			0.09	0.43
			Q4	0.15	0.127	ns			−0.05	0.34
	b:paravermis	Crus I	Avg.	0.12	0.226	ns	0.226	ns	−0.07	0.31
			Q1	−0.11	0.266	ns			−0.32	0.10
			Q2	−0.07	0.462	ns			−0.27	0.13
			Q3	0.20	0.042	*			0.02	0.38
			Q4	0.13	0.183	ns			−0.06	0.32
	c_1:cerebro-cerebellum		Avg.	0.13	0.210	ns	0.226	ns	−0.06	0.31
			Q1	−0.17	0.084	†			−0.36	0.02
			Q2	−0.02	0.862	ns			−0.21	0.19
			Q3	0.21	0.032	*			0.02	0.39
			Q4	0.12	0.221	ns			−0.07	0.31

(*Table continues.*)

Table 7. Continued

Type	Segment/DCN	Lobule	Section	Rho (ρ)	p-value		p-value FDR		95% CI Lower	95% CI Upper
		Crus II	Avg.	0.14	0.178	ns	0.226	ns	−0.05	0.32
			Q1	0.001	0.999	ns			−0.22	0.23
			Q2	−0.09	0.402	ns			−0.28	0.12
			Q3	0.17	0.085	†			−0.01	0.35
			Q4	0.11	0.299	ns			−0.10	0.30
R–R Monosynaptic	Fastigial		Avg.	0.25	0.014	*	0.036	*	0.06	0.41
			Q1	0.18	0.080	†			−0.01	0.35
			Q2	0.25	0.011	*			0.06	0.43
			Q3	0.16	0.123	ns			−0.03	0.33
			Q4	0.11	0.260	ns			−0.08	0.30
	Interposed		Avg.	0.23	0.024	*	0.036	*	0.05	0.39
			Q1	0.18	0.073	†			−0.002	0.35
			Q2	0.23	0.022	*			0.04	0.41
			Q3	0.14	0.156	ns			−0.05	0.32
			Q4	0.08	0.416	ns			−0.12	0.28
	Dentate		Avg.	0.17	0.088	†	0.088	†	−0.02	0.35
			Q1	−0.01	0.948	ns			−0.21	0.19
			Q2	0.11	0.268	ns			−0.09	0.31
			Q3	0.21	0.040	*			0.02	0.38
			Q4	0.08	0.416	ns			−0.11	0.27

Average and segment-wise correlations with the NEO Five-Factor Inventory (NEO-FFI) subscales for neuroticism and agreeableness and fractional anisotropy (FA) values for the right-to-right traveling tracts with the highest densities. The *N* for all correlations is 101, and all confidence intervals are bootstrapped using 10,000 iterations. The degrees of freedom for the main correlations (not controlling for sex) is 99, and the degrees of freedom for partial correlations accounting for sex is 98. False discovery rate (FDR) correction for multiple comparisons was performed for the number of tracts within the polysynaptic (4 tracts) and monosynaptic (3 tracts) correlation domains for overall tract averages, separately. Corrections were not performed for the four quarters, as this was an exploratory analysis used to "drill down" into which portions of the tract were driving the effects where significant or trending associations were uncovered. Note that there was a significant difference between the sexes for each personality trait, so partial correlations are reported in the section. In Extended Data Table 7-1, we check for robustness of results between both the poly- and monosynaptic tractography FA and NEO-FFI measures when accounting for genetic relatedness alone and then together with sex. Significance flags: $^{\dagger}p < 0.10$, $*p < 0.05$, $**p < 0.01$.

Table 8. Quarter-wise brain self-report numeric "heatmap"

Assessment	Variable	Abbrev.	Quarter Q1	Q2	Q3	Q4
R–R polysynaptic: four tracts						
ASR	Anxiety/depression	Anx. Dep	2	2	4	0
	Internalizing	Inter	2	3	4	0
	Social withdrawal	Soc. Withd	4	2	1	0
	Somaticizing	Soma	3	3	3	0
	Attention problems	Attn	1	2	2	0
NEO-FFI	Neuroticism	N	0	2	4	0
	Agreeableness	A	0	0	4	0
	Neuroticism-Ctrl (Sex)	N-Ctrl	0	1	1	0
	Agreeableness-Ctrl (Sex)	A-Ctrl	0	0	3	0
Total			12	14	22	0
Total-Ctrl (Sex)			12	13	18	0
R–R monosynaptic: three tracts						
ASR	Anxiety/depression	Anx. Dep	1	2	1	0
	Internalizing	Inter	1	2	0	0
	Social Withdrawal	Soc. Withd	1	0	0	0
	Somaticizing	Soma	2	2	0	0
	Attention problems	Attn	0	0	0	0
NEO-FFI	Neuroticism	N	1	1	0	0
	Agreeableness	A	2	2	1	0
	Neuroticism-Ctrl (Sex)	N-Ctrl	0	1	0	0
	Agreeableness-Ctrl (Sex)	A-Ctrl	0	2	1	0
Total			8	9	2	0
Total-Ctrl (Sex)			5	9	2	0

A numeric "heatmap" of degree to which each quarter for the brain–behavior analyses is implicated as the driver of the brain self-report effects. For polysynaptic tract investigations, the total possible number of times a single quarter may be significant is four, since there were four polysynaptic tracts under study, while the total number of times a monosynaptic quarter may be significant is three, since only three monosynaptic tracts were under study. For example, a value of "4" in a cell for the polysynaptic tracts would indicate that that quarter was significant in all four polysynaptic tracts for a given brain self-report association. The row titled "Total" represents the total number of times a given quarter was the significant driver of the overall tract average brain self-report associations. The "Total-Ctrl (Sex)" row shows how these results change when controlling for sex in the NEO-FFI correlations. Extended Data Table 8-1 shows how these results change when accounting for genetic relatedness within the sample.

and Snider (1979), who found that paravermal lesions exert chronic effects on forebrain dopamine concentrations. This is interesting in light of our current findings due to the fact that dopamine activity is implicated in a number of psychiatric conditions, as well as in social interest (Homberg et al., 2016). Corroborating our anatomical findings, rodent tracer studies have revealed that most of the projections from the cerebellum to the nucleus accumbens (NAc) by way of the VTA originate in the interposed nucleus and travel ipsilaterally from the cerebellum (Oñate et al., 2023).

The second highest density of streamlines was from the fastigial nucleus. The fastigial, by virtue of it being the output nucleus for the cerebellar vermis, has long been associated with emotion and motivation. Studies in rodents have found connections between the fastigial and periaqueductal gray, amygdala, septal nuclei, and hypothalamus (Heath and Harper, 1974; Snider and Maiti, 1976; Cao et al., 2013; Zhang et al., 2016; Fujita et al., 2020). Rats with lesions to the cerebellar vermis tend to approach natural predators, suggesting that this region is involved in the innate fear response (Supple et al., 1987).

The least robust cerebello-VTA connections in our study were from the largest nucleus in the cerebellum, the dentate nucleus. The ventral dentate consists of projections to association cortices involved in cognitive and sensory processes (Dum and Strick, 2003; Dimitrova et al., 2006; Thurling et al., 2012; Bernard et al., 2014; Palesi et al., 2015, 2021; Steele et al., 2017). Relevant to the work discussed here, Bauer et al. (2011) performed dentate nuclei lesions in rats and found that they exhibited decreased hedonic motivation (Low et al., 2021). Another study showed that deactivation of VTA-projecting dentate neurons attenuated depression symptoms while excitation of this circuit exacerbated depression-like symptoms in stressed mice (Baek et al., 2022).

Relation to preclinical work

We identified robust correlations between spino- and cerebrocerebellar portions of the cerebello-VTA tract and measures of depression symptomology in a normative sample. Our findings echo that of the chemo- and optogenetic rodent literature, especially that by Baek et al. (2022), who found that manipulation of VTA-sending crus I could ameliorate or exacerbate depression-like symptoms. The circuit described in this paper is homologous to our c_1 crus I tract, in which we identified associations with internalizing and social withdrawal.

Our behavioral findings also echo those of Carta et al. (2019), who found that activity between the DCN and VTA was necessary for mice to show a social preference. Interestingly, we found relations between the portions of the cerebello-VTA tract originating in crus I/II and social withdrawal scores on the ASR, a measure that gives an approximation of social interest in humans. Moreover, we found correlations with the portion of this tract that originates in lobule VI of the vermis and agreeableness. While not measuring social interest per se, this construct provides a metric for assessing prosociality, altruism, and cooperation (Wilson et al., 2007), serving as a proxy for adaptive social proclivities that are stable across time (Atherton et al., 2022).

Hierarchy of function by sagittal cerebellar segment

We identified a robust set of correlations between portions of the cerebello-VTA tract (e.g., fastigial and interposed to VTA) and somatic symptoms. This finding hints that sensorimotor and affective capacities may functionally intersect in the cerebellar midline. In the psychiatric literature, it is recognized that cardiovascular function can be perturbed by mood disorders (Bassett, 2016) and anxiety disorders (Trotman et al., 2019). Posture is known to influence mood, such that those who retain an upright stance reap benefits for their general disposition (Awad et al., 2021), and maintain greater feelings of positive emotionality in experimental social stress paradigms (Nair et al., 2015). This is interesting in the context of our findings between FA in nearly identical portions of the cerebello-VTA tract and somatic and attention problems, as it suggests that attending to and interpreting the physiological response to environmental provocation may be necessary for the resultant negative affective appraisal (Dalgleish et al., 2009). In this way, the cerebellum's role in emotion may be in the coupling of emotions to action tendencies and somatic feedback.

Further, there was a bias toward aberrant social processing in higher order, phylogenetically newer portions of the cerebellum, denoted by sagittal segment c_1. Notably, the crus I/II c_1 tracts were the only cerebello-VTA segments associated with social withdrawal symptoms. In this way, there is the suggestion of a mediolateral hierarchy of function, with the phylogenetically older spinocerebellum's role being associated with a more visceral emotional embodiment. Moreover, it is critical to note that the monosynaptic dentate tractography showed a trend in its relationship with social withdrawal, with the quarter resting closest to the dentate (i.e., Q1), driving the trend. There may be a clearer double dissociation in the monosynaptic tractographies' relations with ASR social withdrawal and somaticizing due to the possibility that there may be unique functionalities of the cerebellar cortex identified as the highest-density polysynaptic contributors to cerebello-VTA anatomy. Critically, while this potential hierarchy of function was identified in the ASR measures, it was not found to generalize to NEO-FFI measures of agreeableness, which carries stark social implications.

Limitations

First, our investigation only sought to detail the direct connections between the cerebellum and the VTA. There may be important indirect connections, such as those that may stop first in the red nucleus, thalamus, or hypothalamus. However, animal and human histology have suggested the relevance of the direct connections investigated here (Carta et al., 2019; Baek et al., 2022).

Second, we relied on streamlines as the macrostructural index of interest. Streamlines are known to be confounded by length, curvature, and branching, and may not correspond to tract density per se (Jones et al., 2013; Zhang et al., 2016; Hoffman et al., 2022). The number of streamlines reconstructed using DWI methods may not correspond to the actual number of axonal projections comprising the tract in question. Finally, probabilistic tracking algorithms such as the one employed in this study can be prone to false positive reconstructions (Maier-Hein et al., 2017). Countering this, recent studies have validated diffusion-weighted tracking methods against known anatomy and tracer methods (Dyrby et al., 2007; Sheng et al., 2021; Radwan et al., 2023), much as we did here. Also, the methods used here are more accurate than traditional diffusion tensor imaging approaches (Martinez-Heras et al., 2021).

Third, while we implemented a zebrin-informed partitioning of the posterior cerebellum, the sagittal segments under study do not precisely correspond to true zebrin expression. Our voxel size limited the granularity to chart this with precision. At its core, the sagittal segmentation scheme implemented in the current analysis is best conceptualized as a means of disambiguating spino- versus cerebrocerebellar cortical areas that send projections to distinct output nuclei and may represent a distinct hierarchy of complex behavior.

Lastly, it is important to note that we did not include subjects with failed tract reconstructions in our anatomical analyses, due to our inability to adjudicate between true tract nonexistence or technical shortcomings resulting in reconstruction failure. To discern the cause of failed reconstructions, it is ideal to take an ensemble approach to selecting tracking parameters (Takemura et al., 2016). There are many reasons why tractography may fail, such as due to signal dropout from proximity to CSF, or the selection of suboptimal step-length and curvature parameters. In the future, an ensemble tractography approach that parametrically optimizes these specifications until the ideal combination is achieved should be used to resolve this issue.

References

Amore G, Spoto G, Ieni A, Vetri L, Quatrosi G, Di Rosa G, Nicotera AG (2021) A focus on the cerebellum: from embryogenesis to an age-related clinical perspective. Front Syst Neurosci 15:646052.

Andersson JLR, Jenkinson M, Smith S (2010) Non-linear registration, aka spatial normalisation. In: FMRIB technical report TR07JA2.

Andreasen NC, Pierson R (2008) The role of the cerebellum in schizophrenia. Biol Psychiatry 64:81–88.

Atherton OE, Sutin AR, Terracciano A, Robins RW (2022) Stability and change in the big five personality traits: findings from a longitudinal study of Mexican-origin adults. J Pers Soc Psychol 122:337–350.

Awad S, Debatin T, Ziegler A (2021) Embodiment: I sat, I felt, I performed - posture effects on mood and cognitive performance. Acta Psychol 218: 103353.

Baek SJ, Park JS, Kim J, Yamamoto Y, Tanaka-Yamamoto K (2022) VTA-projecting cerebellar neurons mediate stress-dependent depression-like behaviors. Elife 11:e72981.

Baldacara L, Nery-Fernandes F, Rocha M, Quarantini LC, Rocha GG, Guimaraes JL, Araujo C, Oliveira I, Miranda-Scippa A, Jackowski A (2011) Is cerebellar volume related to bipolar disorder? J Affect Disord 135:305–309.

Bassett D (2016) A literature review of heart rate variability in depressive and bipolar disorders. Aust N Z J Psychiatry 50:511–519.
Bauer DJ, Kerr AL, Swain RA (2011) Cerebellar dentate nuclei lesions reduce motivation in appetitive operant conditioning and open field exploration. Neurobiol Learn Mem 95:166–175.
Bernard JA, Peltier SJ, Benson BL, Wiggins JL, Jaeggi SM, Buschkuehl M, Jonides J, Monk CS, Seidler RD (2014) Dissociable functional networks of the human dentate nucleus. Cereb Cortex 24:2151–2159.
Berridge KC, Robinson TE (2016) Liking, wanting, and the incentive-sensitization theory of addiction. Am Psychol 71:670–679.
Bianciardi M, Toschi N, Eichner C, Polimeni JR, Setsompop K, Brown EN, Hamalainen MS, Rosen BR, Wald LL (2016) In vivo functional connectome of human brainstem nuclei of the ascending arousal, autonomic, and motor systems by high spatial resolution 7-tesla fMRI. MAGMA 29:451–462.
Brambilla P, Barale F, Caverzasi E, Soares JC (2002) Anatomical MRI findings in mood and anxiety disorders. Epidemiol Psichiatr Soc 11:88–99.
Cao BB, Huang Y, Lu JH, Xu FF, Qiu YH, Peng YP (2013) Cerebellar fastigial nuclear GABAergic projections to the hypothalamus modulate immune function. Brain Behav Immun 27:80–90.
Carta I, Chen CH, Schott AL, Dorizan S, Khodakhah K (2019) Cerebellar modulation of the reward circuitry and social behavior. Science 363: eaav0581.
Cohen D (2013) Deep cerebellar nuclei. In: *Encyclopedia of computational neuroscience* (Jaeger D, Jung R, eds), pp 1–4. New York, NY: Springer New York.
Courchesne E, Yeung-Courchesne R, Press GA, Hesselink JR, Jernigan TL (1988) Hypoplasia of cerebellar vermal lobules VI and VII in autism. N Engl J Med 318:1349–1354.
Cuthbert BN, Insel TR (2013) Toward the future of psychiatric diagnosis: the seven pillars of RDoC. BMC Med 11:126.
Dalgleish T, Dunn BD, Mobbs D (2009) Affective neuroscience: past, present, and future. Emot Rev 1:355–368.
DelBello MP, Strakowski SM, Zimmerman ME, Hawkins JM, Sax KW (1999) MRI analysis of the cerebellum in bipolar disorder: a pilot study. Neuropsychopharmacology 21:63–68.
Delis F, Mitsacos A, Giompres P (2013) Lesion of the cerebellar paravermis increases dopamine D1 receptor levels in the contralateral striatum. J Chem Neuroanat 47:35–41.
Delle Chiaie R, Minichino A, Salviati M, Fiorentini S, Tonini A, Bersani FS, De Michele F, Caredda M, Biondi M (2015) Bipolar Spectrum disorders in patients with cerebellar lesions: a comparison with Parkinson's disease. J Nerv Ment Dis 203:725–729.
Dhollander T, Mito R, Raffelt D, Connelly A (2019) Improved white matter response function estimation for 3-tissue constrained spherical deconvolution. In: 27th International Society of Magnetic Resonance in Medicine. Montréal, Québec, Canada.
Dhollander T, Raffelt D, Connelly A (2016) Unsupervised 3-tissue response function estimation from single-shell or multi-shell diffusion MR data without a co-registered T1 image. In: ISMRM Workshop on Breaking the Barriers of Diffusion MRI. Lisbon, Portugal.
Dhollander T, Raffelt D, Connelly A (2018) Accuracy of response function estimation algorithms for 3-tissue spherical deconvolution of diverse quality diffusion MRI data. In: Society of Magnetic Resonance in Medicine. Paris, France.
Diedrichsen J, Balsters JH, Flavell J, Cussans E, Ramnani N (2009) A probabilistic MR atlas of the human cerebellum. Neuroimage 46:39–46.
Diedrichsen J, Maderwald S, Kuper M, Thurling M, Rabe K, Gizewski ER, Ladd ME, Timmann D (2011) Imaging the deep cerebellar nuclei: a probabilistic atlas and normalization procedure. Neuroimage 54:1786–1794.
Dimitrova A, de Greiff A, Schoch B, Gerwig M, Frings M, Gizewski ER, Timmann D (2006) Activation of cerebellar nuclei comparing finger, foot and tongue movements as revealed by fMRI. Brain Res Bull 71:233–241.
Dum RP, Strick PL (2003) An unfolded map of the cerebellar dentate nucleus and its projections to the cerebral cortex. J Neurophysiol 89:634–639.
Dyrby TB, et al. (2007) Validation of in vitro probabilistic tractography. Neuroimage 37:1267–1277.
Eker C, Simsek F, Yilmazer EE, Kitis O, Cinar C, Eker OD, Coburn K, Gonul AS (2014) Brain regions associated with risk and resistance for bipolar I disorder: a voxel-based MRI study of patients with bipolar disorder and their healthy siblings. Bipolar Disord 16:249–261.
Fujita H, Kodama T, du Lac S (2020) Modular output circuits of the fastigial nucleus for diverse motor and nonmotor functions of the cerebellar vermis. Elife 9:e58613.
Glasser MF, et al. (2013) The minimal preprocessing pipelines for the Human Connectome Project. Neuroimage 80:105–124.
Gonen T, Sharon H, Pearlson G, Hendler T (2014) Moods as ups and downs of the motivation pendulum: revisiting reinforcement sensitivity theory (RST) in bipolar disorder. Front Behav Neurosci 8:378.
Heath RG, Harper JW (1974) Ascending projections of the cerebellar fastigial nucleus to the hippocampus, amygdala, and other temporal lobe sites: evoked potential and histological studies in monkeys and cats. Exp Neurol 45:268–287.
Heine SJ, Buchtel EE (2009) Personality: the universal and the culturally specific. Annu Rev Psychol 60:369–394.
Hoffman LJ, Ngo CT, Canada KL, Pasternak O, Zhang F, Riggins T, Olson IR (2022) The fornix supports episodic memory during childhood. Cereb Cortex 32:5388–5403.
Homberg JR, et al. (2016) The role of the dopamine D1 receptor in social cognition: studies using a novel genetic rat model. Dis Model Mech 9:1147–1158.
Jeurissen B, Tournier JD, Dhollander T, Connelly A, Sijbers J (2014) Multi-tissue constrained spherical deconvolution for improved analysis of multi-shell diffusion MRI data. Neuroimage 103:411–426.
Jones DK, Knosche TR, Turner R (2013) White matter integrity, fiber count, and other fallacies: the do's and don'ts of diffusion MRI. Neuroimage 73: 239–254.
Judd EN, Lewis SM, Person AL (2021) Diverse inhibitory projections from the cerebellar interposed nucleus. Elife 10:e66231.
Kim D, Cho HB, Dager SR, Yurgelun-Todd DA, Yoon S, Lee JH, Lee SH, Lee S, Renshaw PF, Lyoo IK (2013) Posterior cerebellar vermal deficits in bipolar disorder. J Affect Disord 150:499–506.
Kong Z, et al. (2022) Somatic symptoms mediate the association between subclinical anxiety and depressive symptoms and its neuroimaging mechanisms. BMC Psychiatry 22:835.
Kruper J, et al. (2021) Evaluating the reliability of human brain white matter tractometry. Apert Neuro 1.
Laidi C, et al. (2015) Cerebellar volume in schizophrenia and bipolar I disorder with and without psychotic features. Acta Psychiatr Scand 131:223–233.
Lippmann S, Manshadi M, Baldwin H, Drasin G, Rice J, Alrajeh S (1982) Cerebellar vermis dimensions on computerized tomographic scans of schizophrenic and bipolar patients. Am J Psychiatry 139:667–668.
Low AYT, et al. (2021) Reverse-translational identification of a cerebellar satiation network. Nature 600:269–273.
Lupo M, Olivito G, Gragnani A, Saettoni M, Siciliano L, Pancheri C, Panfili M, Bozzali M, Delle Chiaie R, Leggio M (2021) Comparison of cerebellar grey matter alterations in bipolar and cerebellar patients: evidence from voxel-based analysis. Int J Mol Sci 22:3511.
Maier-Hein KH, et al. (2017) The challenge of mapping the human connectome based on diffusion tractography. Nat Commun 8:1349.
Marcus DS, et al. (2013) Human Connectome Project informatics: quality control, database services, and data visualization. Neuroimage 80:202–219.
Marcus DS, Harwell J, Olsen T, Hodge M, Glasser MF, Prior F, Jenkinson M, Laumann T, Curtiss SW, Van Essen DC (2011) Informatics and data mining tools and strategies for the human connectome project. Front Neuroinform 5:4.
Martinez-Heras E, Grussu F, Prados F, Solana E, Llufriu S (2021) Diffusion-weighted imaging: recent advances and applications. Semin Ultrasound CT MR 42:490–506.
McCrae RR, Costa PT Jr (2004) A contemplated revision of the NEO five-factor inventory. Pers Individ Dif 36:587–596.
Metoki A, Wang Y, Olson IR (2022) The social cerebellum: a large-scale investigation of functional and structural specificity and connectivity. Cereb Cortex 32:987–1003.
Mills NP, Delbello MP, Adler CM, Strakowski SM (2005) MRI analysis of cerebellar vermal abnormalities in bipolar disorder. Am J Psychiatry 162: 1530–1532.
Miquel M, Gil-Miravet I, Guarque-Chabrera J (2020) The cerebellum on cocaine. Front Syst Neurosci 14:586574.
Moberget T, et al. (2018) Cerebellar volume and cerebellocerebral structural covariance in schizophrenia: a multisite mega-analysis of 983 patients and 1349 healthy controls. Mol Psychiatry 23:1512–1520.
Monkul ES, Hatch JP, Sassi RB, Axelson D, Brambilla P, Nicoletti MA, Keshavan MS, Ryan ND, Birmaher B, Soares JC (2008) MRI study of the cerebellum in young bipolar patients. Prog Neuropsychopharmacol Biol Psychiatry 32:613–619.

Morales I, Berridge KC (2020) 'Liking' and 'wanting' in eating and food reward: brain mechanisms and clinical implications. Physiol Behav 227:113152.
Moulton EA, Elman I, Becerra LR, Goldstein RZ, Borsook D (2014) The cerebellum and addiction: insights gained from neuroimaging research. Addict Biol 19:317–331.
Nair S, Sagar M, Sollers J 3rd, Consedine N, Broadbent E (2015) Do slumped and upright postures affect stress responses? A randomized trial. Health Psychol 34:632–641.
Nasrallah HA, McCalley-Whitters M, Jacoby CG (1982) Cerebral ventricular enlargement in young manic males. A controlled CT study. J Affect Disord 4:15–19.
Novello M, Bosman LWJ, De Zeeuw CI (2022) A systematic review of direct outputs from the cerebellum to the brainstem and diencephalon in mammals. Cerebellum 23:210–239.
Oñate M, Vera J, Khatami L, Khodakhah K (2023) Neuroanatomical characterization of cerebellar inputs to the dopamine centers in the midbrain. In: Gordan Research Conference. Lewiston, ME, United States.
Palesi F, Ferrante M, Gaviraghi M, Misiti A, Savini G, Lascialfari A, D'Angelo E, Gandini Wheeler-Kingshott CAM (2021) Motor and higher-order functions topography of the human dentate nuclei identified with tractography and clustering methods. Hum Brain Mapp 42:4348–4361.
Palesi F, Tournier JD, Calamante F, Muhlert N, Castellazzi G, Chard D, D'Angelo E, Wheeler-Kingshott CA (2015) Contralateral cerebello-thalamo-cortical pathways with prominent involvement of associative areas in humans in vivo. Brain Struct Funct 220:3369–3384.
Perciavalle V, Berretta S, Raffaele R (1989) Projections from the intracerebellar nuclei to the ventral midbrain tegmentum in the rat. Neuroscience 29: 109–119.
Phillips JR, Hewedi DH, Eissa AM, Moustafa AA (2015) The cerebellum and psychiatric disorders. Front Public Health 3:66.
Phillipson OT (1979) Afferent projections to the ventral tegmental area of Tsai and interfascicular nucleus: a horseradish peroxidase study in the rat. J Comp Neurol 187:117–143.
Pizzagalli DA (2014) Depression, stress, and anhedonia: toward a synthesis and integrated model. Annu Rev Clin Psychol 10:393–423.
Popal HS (2023) Pinpointing the role of the cerebellum in social reward processing. In: *Psychology and neuroscience*. Philadelphia: Temple University.
Purves D, Augustine GJ, Fitzpatrick D (2001) Circuits within the cerebellum. In: *Neuroscience* (Purves D, Augustine GJ, Fitzpatrick D, eds), Ed 2. Sunderland, MA: Sinauer Associates.
Radwan AM, Emsell L, Vansteelandt K, Cleeren E, Peeters R, Vleeschouwer D, Theys T, Dupont P, Sunaert S (2023) A comparison of diffusion MRI presurgical tractography techniques with intraoperative mapping-based validation. In. medRxiv.
Rajasekhar SSSN (2022) Anatomy of cerebellum. In: *Spinocerebellar ataxia - concepts, particularities and generalities* (Ambrosi PB, ed). IntechOpen. Available at: https://www.intechopen.com/chapters/76566
Russo SJ, Nestler EJ (2013) The brain reward circuitry in mood disorders. Nat Rev Neurosci 14:609–625.
Sheng Z, et al. (2021) Constrained-spherical deconvolution tractography in the evaluation of the corticospinal tract in glioma surgery. Front Surg 8: 646465.
Snider RS, Maiti A (1976) Cerebellar contributions to the Papez circuit. J Neurosci Res 2:133–146.
Snider RS, Maiti A, Snider SR (1976) Cerebellar pathways to ventral midbrain and nigra. Exp Neurol 53:714–728.
Snider SR, Snider RS (1979) Kainic acid: enduring alterations in cerebellar morphology and in cerebral catecholamine and GABA concentrations after cerebellar injection in the rat. Neurosci Lett 12:339–342.
Snyder HR, Silton RL, Hankin BL, Smolker HR, Kaiser RH, Banich MT, Miller GA, Heller W (2023) The dimensional structure of internalizing psychopathology: relation to diagnostic categories. Clin Psychol Sci 11: 1044–1063.
Sotiropoulos SN, et al. (2013) Advances in diffusion MRI acquisition and processing in the Human Connectome Project. Neuroimage 80:125–143.
Steele CJ, Anwander A, Bazin PL, Trampel R, Schaefer A, Turner R, Ramnani N, Villringer A (2017) Human cerebellar sub-millimeter diffusion imaging reveals the motor and non-motor topography of the dentate nucleus. Cereb Cortex 27:4537–4548.
Supple WF Jr, Leaton RN, Fanselow MS (1987) Effects of cerebellar vermal lesions on species-specific fear responses, neophobia, and taste-aversion learning in rats. Physiol Behav 39:579–586.
Takemura H, Caiafa CF, Wandell BA, Pestilli F (2016) Ensemble tractography. PLoS Comput Biol 12:e1004692.
Thurling M, Hautzel H, Kuper M, Stefanescu MR, Maderwald S, Ladd ME, Timmann D (2012) Involvement of the cerebellar cortex and nuclei in verbal and visuospatial working memory: a 7 T fMRI study. Neuroimage 62:1537–1550.
Trotman GP, Veldhuijzen van Zanten J, Davies J, Moller C, Ginty AT, Williams SE (2019) Associations between heart rate, perceived heart rate, and anxiety during acute psychological stress. Anxiety Stress Coping 32:711–727.
Ugurbil K, et al. (2013) Pushing spatial and temporal resolution for functional and diffusion MRI in the human connectome project. Neuroimage 80:80–104.
Unverdi M, Alsayouri K (2023) Neuroanatomy, cerebellar dysfunction. In: *StatPearls* [Internet]. Treasure Iland, FL: StatPearls Publishing.
Van Essen DC, et al. (2012) The human connectome project: a data acquisition perspective. Neuroimage 62:2222–2231.
Van Essen DC, Smith SM, Barch DM, Behrens TE, Yacoub E, Ugurbil K, WU-Minn HCP Consortium (2013) The WU-Minn Human Connectome Project: an overview. Neuroimage 80:62–79.
Wang SS, Kloth AD, Badura A (2014) The cerebellum, sensitive periods, and autism. Neuron 83:518–532.
Watabe-Uchida M, Zhu L, Ogawa SK, Vamanrao A, Uchida N (2012) Whole-brain mapping of direct inputs to midbrain dopamine neurons. Neuron 74:858–873.
Watson D, Naragon-Gainey K (2010) On the specificity of positive emotional dysfunction in psychopathology: evidence from the mood and anxiety disorders and schizophrenia/schizotypy. Clin Psychol Rev 30:839–848.
Wilson RS, Schneider JA, Arnold SE, Bienias JL, Bennett DA (2007) Conscientiousness and the incidence of Alzheimer disease and mild cognitive impairment. Arch Gen Psychiatry 64:1204–1212.
Yeatman JD, Dougherty RF, Myall NJ, Wandell BA, Feldman HM (2012) Tract profiles of white matter properties: automating fiber-tract quantification. PLoS One 7:e49790.
Zhang XY, Wang JJ, Zhu JN (2016) Cerebellar fastigial nucleus: from anatomic construction to physiological functions. Cerebellum Ataxias 3:9.